THE DYNAMIC MEASUREMENT OF UNMANNED AERIAL VEHICLE RADAR CROSS SECTION

MESURER DYNAMIQUEMENT LA SURFACE EQUIVALENTE RADAR DE DRONES

A Thesis Submitted to the Division of Graduate Studies
of the Royal Military College of Canada
by

Rudy Guay, BEng, rmc
Captain

In Partial Fulfillment of the Requirements for the Degree of
Master of Applied Science in Electrical Engineering

April, 2016

© This thesis may be used within the Department of National Defence
but copyright for open publication remains the property of the author.

Cette thèse est dédiée à mes parents, Monelle et Robert. Leurs multiples sacrifices et encouragements au fil des ans sont les fondations de ce document. This thesis is also dedicated to my other half, Abbey, for her unwavering support during its day-to-day writing.

Acknowledgements

This thesis would not have been possible without the outstanding support and guidance of Dr. Joey Bray, whose performance as a thesis supervisor made this research conceivable. Special thanks to Dr. Germain Drolet for his help with statistical methods. Additional thanks to Dr. Romulo Lins for his help with 3D modeling and printing, as well as his expertise in solving issues with the infrared camera system. Thank you as well to Dr. Sidney Givigi and Dr. Alain Beaulieu for the unrestricted use of the robotic laboratory resources. Finally, my sincere appreciation to the staff of the Director Technical Airworthiness & Engineering Support 8 for their generous funding.

Abstract

The radar cross-section (RCS) is a key parameter used to determine whether or not an airborne target will be detected by a radar at a given range. The accurate measurement of the RCS is of particular importance for the detection of miniature unmanned aerial vehicles (UAV) because the radar return strength is low. Although the UAV's RCS may be determined statically in an anechoic chamber, it may be advantageous to measure it whilst the target is in motion due to the greater resemblance with an operational environment. However, the dynamic measurement of RCS adds complexity to the measurement system because of the requirement to track the UAV in-flight. Furthermore, vibrations and moving parts modulate the return echo, which implies that the RCS can only be characterized statistically.

This work describes the design of the Dynamic RCS Measurement System used to measure the RCS of UAVs flying indoors. The results of measurements of a test UAV and comparison with static measurements show that the Dynamic RCS Measurement System is a viable option to investigate how dynamic effects affect the RCS of a flying UAV and to compute probabilities of detection.

Résumé

La surface équivalente radar (SER) est un paramètre important pour déterminer si une cible va être détectée par un radar à une certaine portée. La SER est particulièrement importante pour la détection de petits drones, car la puissance du retour radar est faible. La SER peut être déterminée statiquement dans une chambre anéchoïque. Il peut néanmoins être avantageux de la mesurer lorsque la cible est mobile en raison de la plus grande ressemblance avec un environnement opérationnel. Cependant, mesurer dynamiquement la SER ajoute de la complexité au système de mesure en raison de la nécessité de traquer le drone en vol. De plus, les vibrations et pièces mobiles du drone modulent le retour radar. Ceci implique que la SER peut seulement être caractérisée statistiquement.

Ce travail décrit le système de mesure de la SER dynamique qui est utilisé pour mesurer la SER de drones volant à l'intérieur. Les résultats obtenus en testant le système montrent qu'il est une option viable pour déterminer l'impact des effets dynamiques sur la SER d'un drone en vol et pour calculer des probabilités de détection.

Contents

List of Tables

List of Figures

List of Acronyms

ACF	Auto Correlation Function
AIC	Akaike Information Criterion
CDF	Cumulative Distribution Function
CEM	Computational Electromagnetic
CPI	Coherent Pulse Interval
DF	Duty Factor
Dyn	Dynamic
FEM	Finite Element Method
Freq	Frequency
ISAR	Inverse Synthetic Aperture Radar
LRT	Likelihood Ration Test
LVRTS	LabVolt^{TM} Radar Training System
MLE	Maximum Likelihood Estimation
PDF	Probability Density Function
PO	Physical Optics
PoD	Probability of Detection
PRF	Pulse Repetition Frequency
PWM	Pulse Width Modulation
RAM	Radio Absorbent Material
RCS	Radar Cross Section
RMCC	Royal Military College of Canada
SCNR	Signal-to-Clutter and Noise Ratio
SNR	Signal-to-Noise Ratio
UAV	Unmanned Aerial Vehicle
Var	Variance

List of Symbols

σ	RCS [m^2 or dBsm]
	Lognormal PDF scale
R	Range [m]
$\overrightarrow{E}_{scat}$	Scattered electric field strength [V/m]
$\overrightarrow{E}_{inc}$	Incident electric field strength [V/m]
R_{max}	Maximum detectable range
P_t	Transmitted power [W]
G	Gain
λ	Wavelength [m]
	Weibull PDF scale
P_{min}	Minimum detectable power in receiver [W]
ϕ	UAV yaw angle [rad]
θ	UAV pitch angle [rad]
$\Delta R_{cross-range}$	Cross-range resolution of ISAR image
$\Delta\phi_{isar}$	Total yaw angle variation of UAV during ISAR measurement [rad]
ΔR_{range}	Range resolution of ISAR image [m]
c	Speed of light [m/s]
f	Frequency [Hz]
Δf	Frequency sweep width of the network analyzer [Hz]
p	Probability density function
a	Gamma PDF shape
b	Gamma PDF scale
σ_{RCS}	RCS [m^2]
μ	Lognormal PDF location
k	Weibull PDF shape
	Number of yaw bins
β	Exponential PDF mean
L	Likelihood function

θ_p	Vector of PDF parameters
q	Number of independent PDF parameters
$\Delta\phi_{decor}$	ACF decorrelation angle [rad]
L_{scat}	Length of scatterers line array in ACF estimation [m]
F	Cumulative distribution function
$\bar{x}$	Average SNR
P_{FA}	Probability of False Alarm
P_{noise}	Noise power in receiver [W]
$\Delta\phi_{res}$	Yaw angular resolution in static measurements [deg]
L_{pulse}	Length of correlation square pulse [m]
L_{target}	Maximum length of target [m]
$rect$	Rectangular correlation pulse
p_r	Received power signal [W]
I	In-phase radar signal [V]
Q	Quadrature-phase radar signal [V]
y	RCS [m^2]
ϵ	Error
Y	Random variable representing the full-UAV RCS [m^2]
X	Random variable representing the RCS in a bin [m^2]

1 Introduction

1.1 Background

Recent years have seen a rise in the use of unmanned aerial vehicles (UAV). They can be used for a multitude of civilian applications, including meteorology studies, disaster relief, agricultural monitoring, and surveillance [2]. In a military environment, a UAV may carry any type of light payload, from a jammer to an explosive device, or may be used for reconnaissance [2].

Until recently, military organizations were primarily concerned with detecting fixed-wing drones which have a radar cross section (RCS) comparable to a manned vehicle. However, mini-UAVs are increasingly used to penetrate sensitive areas. Two examples are a Parrot^{TM} AR.Drone landing a few feet from the German Chancellor at a campaign event in 2013 and a DJI Phantom^{TM} quadcopter crashing on the White House lawn in 2015 [3].

The first step to counteract the mini-UAV threat is detection. Two examples of anti-UAV systems are the Falcon Shield from Selex ES^{TM} and the new counter-UAV system from Airbus^{TM} Defense and Space that both use radar detectors. However, because of their small radar cross-section (RCS) and their ability to fly very low into the radar clutter, UAVs are difficult to detect [4].

The probability of detecting a UAV at a given range is dependent on the accurate knowledge of its in-flight RCS [5]. Curves of the probability of detection versus the range may be used to select the radar configuration that optimizes the probability of detection [6]. Conversely, these curves may be used by a UAV operator to select an optimal route to avoid detection by an enemy radar.

1.2 Problem Statement

A current methodology to determine the RCS of a UAV is to measure the radar return statically in a controlled environment such as an anechoic chamber. Similarly, computer simulations may be used. However, UAVs are often built using non-metallic parts, making simulating the RCS very costly in time and computer memory [7]. Both methods, static measurement and simulations, determine the RCS of the UAV statically, while it is at rest. The results may not be representative of operational conditions due to airframe vibrations, distortion and the rotation of engine parts [8].

The use of the static RCS to determine the probability of detection of a UAV may result in inaccurate results [9]. Unfortunately, the measurement of the in-flight RCS of a UAV requires tracking the target while it is airborne [6]. The added complexity of this method may prohibit its use. However, considering the low RCS of miniature UAVs, knowledge of the dynamic RCS may be necessary to accurately determine the probability of detection and increase the detection range to acceptable levels through optimal radar configuration.

1.3 Thesis Statement

The dynamic RCS of a mini-UAV may be significantly different than its static RCS. The objective of this research is to build a system capable of measuring the dynamic RCS of small UAVs and to use the system to measure the RCS of the Parrot^{TM} AR.Drone. The statistically characterized dynamic RCS will be compared to measured and simulated static RCS values.

1.4 Methodology

As described in [9], the preferred way to obtain RCS measurements from a target is in its operational environment. In the case of a UAV, this implies measuring its RCS while it is flying. This requirement adds considerable complexity to the measurement system because it also implies that the radar must track the target simultaneously while measuring its RCS. Furthermore, a mechanism must be in place to associate the measured RCS with the illuminated target aspect angle. To overcome both problems, a combination of available radar technology and infrared tracking equipment will be used.

The first step of this thesis is to statically measure the RCS of AR.Drone using conventional methods. Electromagnetic simulations and measurements within an anechoic chamber will be used to determine the UAV's RCS.

The second step is to design and build a new Dynamic RCS Measurement System. The system will merge the LabVolt™ Radar Training System (LVRTS) and the Optitrack™ Tracking Tool Infrared System using Matlab™ scripts to measure dynamically the RCS of the Parrot™ AR.Drone UAV. The infrared system will be used to track the UAV in-flight and determine the illumination angle. The dynamic system will be validated by taking static measurements of a stationary target that will be supported by a custom-made low-RCS pylon. The results will then be compared with the RCS obtained using conventional methods.

The third step of this thesis is the statistical analysis of the dynamic RCS measurements of the UAV. Various statistical methods will be used to reduce the data sets to useful results.

The final step is the comparison of the dynamically obtained RCS with the static measurements. The data sets will be compared and conclusions will be made as to the equivalence of both methods.

1.5 Thesis Outline

Chapter 2 provides an introduction to RCS. It presents the definition of the RCS and how it is measured or simulated in a static environment. It discusses how the RCS is modeled statistically with the use of a probability density function (PDF). Then, it highlights the methodology used for dynamic measurements. Finally, it shows how the RCS is used to compute the probability that a target is detected by a radar as a function of range.

Chapter 3 describes the methods used to compute and measure the static RCS of the AR.Drone using computer simulations and anechoic chamber measurements. Results are presented and both methods are compared.

Chapter 4 presents the proposed Dynamic RCS Measurement System which is used to dynamically measure the RCS of small UAVs in a laboratory environment. Static measurements are taken and compared to anechoic chamber measurements to validate the design.

Chapter 5 presents the configuration and calibration of the Dynamic RCS Measurement System. Results obtained for a dynamic measurement campaign of the AR.Drone are presented. Multiple statistical methods are used and compared to obtain a PDF for the UAV and to compute its probabilities of detection. Comparisons are also made between the static and dynamic measurements.

Chapter 6 offers the conclusion of the thesis and presents areas of further research in the dynamic measurement of a small UAV RCS.

2 Literature Survey

2.1 Radar Cross-Section Definition

The RCS (σ) is a measure of the electromagnetic (EM) reflective strength of a target. It can be thought of as the hypothetical area in square meters of an isotropic radiator that would produce the same echo power at the radar as the target [10]. It is defined as:

$$\sigma = \lim_{R \to \infty} 4\pi R^2 \frac{|\overrightarrow{E}_{scat}|^2}{|\overrightarrow{E}_{inc}|^2} \tag{2.1}$$

where $\overrightarrow{E}_{inc}$ is the incident electric field evaluated at the target, $\overrightarrow{E}_{scat}$ is the scattered field evaluated at the radar and R is the range. The fact that the range tends towards infinity implies that the incident and reflected waves must be plane waves. However, a common approximation is to place the target in the far field of the antenna, and vice versa [11]. Conceptually, the RCS is the product of the geometrical cross section, the reflectivity, and directivity of the target [12]. The RCS is a function of many factors including the target's aspect angle with respect to the incident wave, the frequency and the polarization.

If the radar transmitter and receiver are collocated, the RCS is called monostatic, otherwise it is bistatic. The RCS is a key component of the monostatic radar range equation:

$$R_{max} = \sqrt[4]{\frac{P_t G^2 \lambda^2 \sigma}{P_{min}(4\pi)^3}} \tag{2.2}$$

where R_{max} is the maximum detection range, P_t is the transmitted power, G is the antenna gain, λ is the free-space wavelength and P_{min} is the minimum power detectable in the receiver [13]. The equation shows that the maximum detection range is proportional to the fourth root of the RCS. As such, a sixteen-fold increase of the RCS is necessary to double the detection range.

2.2 RCS Simulation

A cost effective way to determine a target's static RCS is to use numerical methods embedded in simulation software [11]. The RCS is considered static because the target is stationary, including its propellers and engine parts. Numerical methods that solve Maxwell's equations are called full-wave methods. They are the preferred choice because they give an exact solution for the electric and magnetic fields. However, because of the high computational cost of solving the equations, approximative methods have been developed in tandem. This section will provide an overview of the different approaches used in this thesis.

2.2.1 Full-Wave Method

The Finite Element Method (FEM) is a full-wave method that discretizes the target space, including surrounding air, into a set of tetrahedrons. The unknown quantities are the electric fields within each element. These fields are approximated using a local function that, when substituted in the differential form of Maxwell's equations, transforms them into a linear matrix equation. Because the resulting matrix is sparse, it can be solved using an efficient sparse matrix solver. Reference [7] describes the technique and its implementation into a commercially licensed computational electromagnetic (CEM) software called HFSS^{TM}. The main drawback of FEM is the need to model the surrounding air. Because it is not possible to model an infinite quantity of air, the target space must be terminated with an Absorbing Boundary Condition (ABC). The complexity of the ABC will influence the final result. For example, HFSS^{TM} allows the user to choose between a first order ABC and the Perfectly Matched Layer (PML). The choice of ABC is influenced by the geometry of the target and has an impact on the computational load and quality of the simulated RCS results. FEM is very robust and allows for the simulation of complex dielectric materials [7].

2.2.2 High Frequency Asymptotic Methods

High-frequency asymptotic methods may be used when the incident wavelength is at least 3 times smaller than the target dimensions [13]. These methods do not compute exact solutions to Maxwell's Equations, but are based on approximations to reduce the computational loads. Although full-wave methods are preferable, they are usually not feasible for complex targets, hence the need for asymptotic methods.

Physical Optics (PO) is a current-based asymptotic method used to evaluate the scattered fields for a perfectly conductive target. PO approximates the currents at each surface mesh with those present when the surface is flat at the point of incidence [10]. Furthermore, each mesh is treated in isolation. The scattered fields are calculated using surface integration and Green's free space function. PO is most accurate for incident angles smaller than 30 degrees for a perfectly conductive target [1]. Figure 2.1 shows the vertically polarized (VV) RCS at 8 GHz versus the yaw angle of the POFACETs^{TM} model helicopter simulated using the free physical optics Software [14].

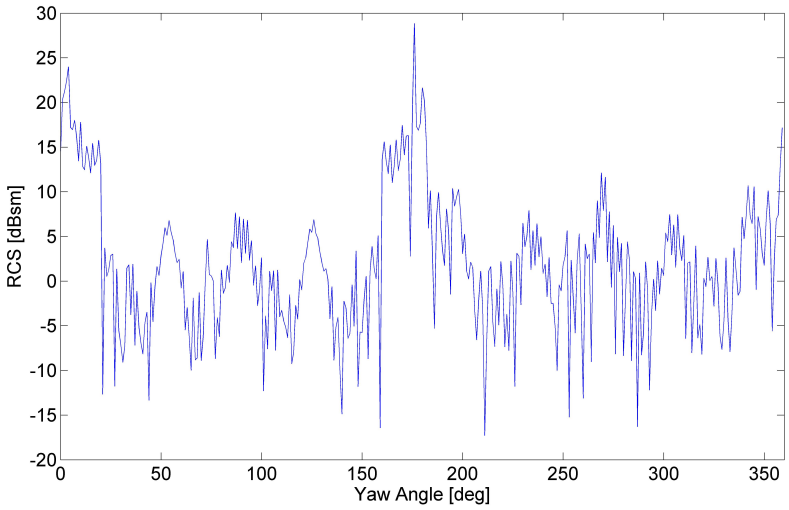

Figure 2.1: RCS versus yaw angle of a helicopter

2.3 Static RCS Measurements

Simulation allows the estimation of a target's RCS efficiently and at low cost. However, measurements are necessary to validate the results or to obtain more realistic values that account for model simplifications and manufacturing imperfections.

A common way of measuring the RCS statically is to mount the target on a low-RCS pylon and rotate it with respect to an illuminating radar, as shown in Figure 2.2. Returns are measured and the RCS is computed for each aspect angle. To mitigate unwanted reflections from the background,

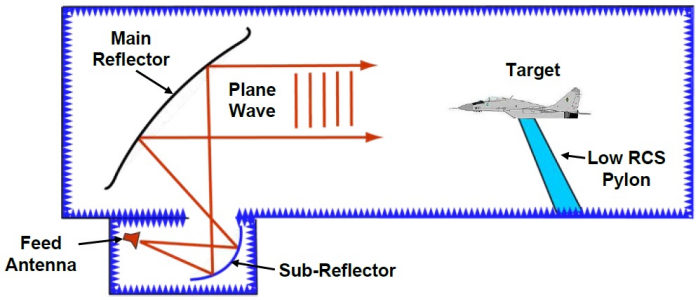

Figure 2.2: Compact range anechoic chamber configuration for RCS measurements [1]

measurements are often taken in an anechoic chamber. However, background subtraction techniques may also be used instead, as described in [15]. The RCS is considered static because the target is not in flight, which makes the RCS deterministic.

Reference [16] describes the measurement concept when using the HP8510 Network Analyzer. With the HP8510 configured in swept frequency mode, the transmit antenna is connected to port 1 and the receive antenna is connected to port 2. For every frequency increment, a reading of the transmission coefficient (s_{21}) is made. Averaging is used for every frequency to increase the signal-to-noise ratio (SNR). Because amplitude and phase are measured, it is possible to take the Inverse Discrete Fourier Transform to obtain the time-domain signal. Time-gating may then be used to remove clutter. A wider frequency bandwidth corresponds to a shorter illuminating pulse, improving the range resolution.

Despite the use of an anechoic chamber, unwanted residual reflections still exist and must be removed by calibrating the equipment. A common way to subtract the undesirable reflections is to measure the anechoic chamber without the target and then to subtract the result from the measurements using a vector subtraction [16].

To calibrate the chamber, the return from a reference object such as a perfect electrical conductor (PEC) sphere of known RCS is measured and the resulting transmission coefficient (s_{21}) is associated with the theoretical RCS value. The use of an anechoic chamber with precise calibration allows high precision RCS measurements to be made of small targets with a network analyzer. As an example, a styrofoam column with a 3 inch radius was measured 30 dB above the noise floor between 0.6 and 4.6 GHz [16].

2.3.1 Inverse Synthetic Aperture Radar Imaging

Measurements using a vector analyzer within an anechoic room may also be used to generate a 2-dimensional inverse synthetic aperture radar (ISAR) image of the target. An inverse Fourier transform converts the measured frequency-domain signal into the time domain. The target is then rotated and the process is repeated. Once all time-domain signals have been acquired, a spatial Fourier transform is used to produce a high-resolution image [17].

The cross-range resolution $\Delta R_{cross-range}$ in meters is given by:

$$\Delta R_{cross-range} = \frac{\lambda}{2\Delta\phi_{isar}} \tag{2.3}$$

where $\Delta\phi_{isar}$ is the total variation of the target yaw angle in radians and λ is the wavelength in meters that corresponds to the middle frequency of the network analyzer frequency sweep [17].

The range resolution ΔR_{range} in meters is given by:

$$\Delta R_{range} = \frac{1.95c}{2\Delta f} \tag{2.4}$$

where c is the speed of light in m/s and Δf is the frequency sweep width of the network analyzer in Hz [18].

Although the rotation of the UAV implies that the image coordinate system is spherical, for small rotation angles $\Delta\phi_{isar}$, the small angle approximation may be used to form the image directly in Cartesian coordinates [19].

2.4 Statistical Modeling of Static RCS

The RCS of a static target is a deterministic function that varies significantly with polarization, frequency and aspect angle. As can be seen from Figure 2.1, the RCS as a function of aspect angle is a complicated function with a large dynamic range. Furthermore, an operational radar does not know the exact orientation of the target. Therefore the RCS is often treated as a random variable in radar range calculations. The RCS histogram may be calculated by counting the number of occurrences of each RCS value in the RCS function. Figure 2.3 shows the RCS histogram for the RCS function of Figure 2.1. A probability density function (PDF) may then fitted to the histogram. Another approach is to use Maximum Likelihood Estimation (MLE) techniques. Notwithstanding the approach to determine the PDF, the curve of Figure 2.1 can be simply represented by a set of PDF parameters (usually one or two, depending on the type of PDF).

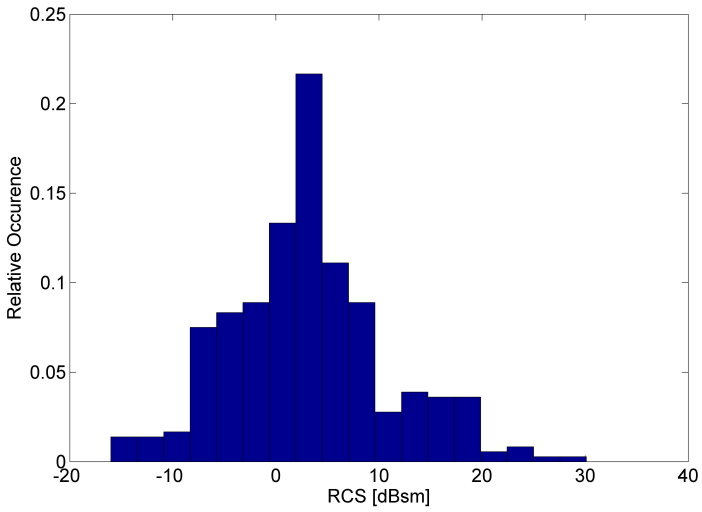

Figure 2.3: RCS distribution of helicopter

Radar returns are often coherently integrated to increase the signal strength and minimize noise. However, the RCS PDF alone does not give an indication of how long returns may be integrated. The Auto Correlation Function (ACF) provides that information. The combination of a PDF and ACF gives the target fluctuation model [13].

2.4.1 The Probability Density Function of Fluctuating Targets

To model complex targets, it is convenient to fit a PDF over the RCS distribution, thereby reducing the number of data points and easing further computations. Many PDFs may be considered for this, all of which are only defined for positive RCS ($\sigma > 0$). A commonly used PDF is the Gamma PDF given by:

$$p(\sigma; a, b) = \frac{e^{\frac{-\sigma}{b}} \sigma^{a-1}}{b^a \Gamma(a)} \tag{2.5}$$

where σ is the RCS, a and b are free parameters and Γ is the Gamma function [13].

The Lognormal PDF is often used to represent the RCS of stealthy targets [20]. The PDF is given by:

$$p(\sigma_{RCS};\mu,\sigma) = \frac{1}{\sigma_{RCS}\sigma\sqrt{2\pi}} e^{-\frac{(\ln\sigma_{RCS}-\mu)^2}{2\sigma^2}} \tag{2.6}$$

where σ_{RCS} is the RCS, μ is the location and σ is the scale. The symbol σ_{RCS} is used solely in this equation to help distinguish the RCS from the scale parameter. RCS measurements around the nose area of a F-4 Phantom show that its RCS is best represented by the Lognormal PDF [9].

The Weibull PDF is also sometimes used to model targets [13]. The PDF is given by:

$$p(\sigma;\lambda,k) = \frac{k}{\lambda}(\frac{\sigma}{\lambda})^{k-1} e^{-(\sigma/\lambda)^k} \tag{2.7}$$

where λ is the scale and k is the shape parameter.

The Gamma, Lognormal and Weibull PDF have two free parameters. Other PDFs like the Exponential only have a single parameter. The Exponential PDF is given by:

$$p(\sigma;\beta) = \frac{1}{\beta} e^{-\frac{\sigma}{\beta}} \tag{2.8}$$

where β is the mean of the PDF [13]. The exponential PDF is used in the Swerling Target Models [13].

Figure 2.4 shows the Gamma, Lognormal and Weibull PDFs with a mean of 4 and a variance of 2.

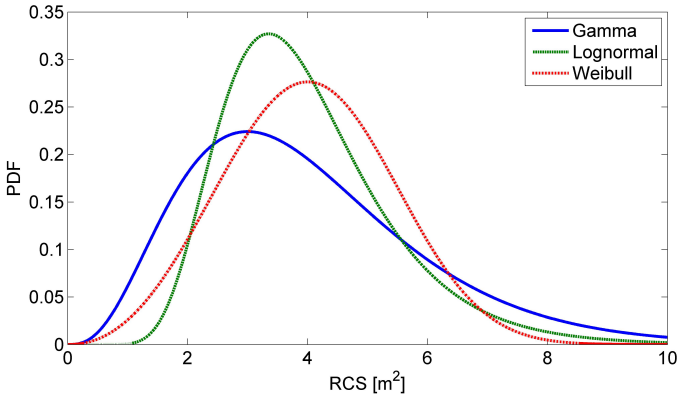

Figure 2.4: PDF examples with same mean and variance

Selection of Best-Fitting PDF

Different PDFs may be used to statistically characterize the RCS of a target. The likelihood function determines how well the data fits a PDF with given parameters [21]. By maximizing the likelihood function, the most likely PDF to have yielded the measurements may be selected. The likelihood function is given by:

$$L(\theta_p) = \prod_{i=1}^{n} p(\sigma_i; \theta_p) \tag{2.9}$$

where n is the number of measurements, σ_i are the measured RCS values that we are seeking a PDF for and θ_p are the PDF parameters (for example, σ and μ for a lognormal PDF).

The likelihood function should be computed for many different PDF type (lognormal, Weibull, etc.). However, relying solely on the likelihood function will usually result in the selection of the PDF with the most independent parameters. To avoid over-fitting, the Akaike Information Criterion (AIC) introduces a cost for each additional parameter used and is given by:

$$AIC = -2 \ln L(\hat{\theta}) + 2q \tag{2.10}$$

where $L(\hat{\theta})$ is the maximal value of the likelihood function and q is the number of independent parameters [21]. To determine the most likely PDF for an RCS distribution, we start by selecting the parameters of each desired type of PDF (Gamma, Weibull, etc) by maximizing their respective likelihood function, and then we compute the AIC for each PDF type. The PDF with the minimal AIC score is the selected PDF.

For example, fitting different types of PDF on the RCS of the helicopter of Figure 2.1 results in selecting a lognormal PDF with parameters μ of 0.437 and σ of 1.76. Table 2.1 lists the computed AIC values.

Table 2.1: PDF Fitting of the Helicopter Model

PDF Type	**AIC**
Lognormal	1750
Gamma	1982
Weibull	1854
Exponential	2383

In this scenario, the cost of each additional parameter is low when compared to the AIC score. However, the results of Section 5.3.1 will show AIC scores more closely spaced for the AR.Drone.

Accuracy of Fit

The AIC score allows to choose a PDF and its parameters, but it is based on a single number that does not provide an indication of how well the selected PDF fits the data, just which one is best among a pre-selected list of candidate PDFs. A quantile-quantile plot may be used to graphically judge how well the data actually fits. Figure 2.5 plots the measured quantiles versus the quantiles of the fitted lognormal for the POFACETs^{TM} helicopter. For a perfect match, the markers should be exactly aligned with the straight line. Despite being the most likely PDF, the data fits the model well only for the smaller quantiles and the correlation degrades for the higher quantiles. Thus, a low AIC score doesn't necessarily imply a good fit.

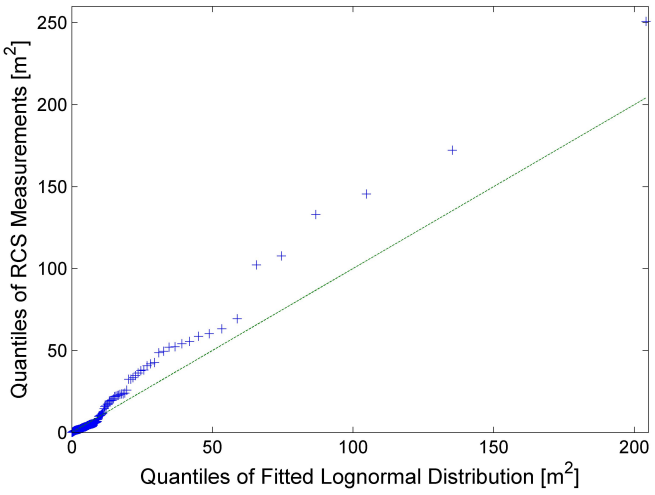

Figure 2.5: QQ plot of POFACETs^{TM} helicopter

Sensitivity of Fit

The QQ plot allows one to visually determine how well the measurements fit the selected PDF, but it does not give an indication of how sensitive the

parameter selection is. The likelihood ratio test (LRT) allows one to determine a 95% confidence interval of the parameters of θ_p using the inequation:

$$-2 \ln \frac{L(\theta_p)}{L(\hat{\theta}_p)} < \chi^2_{(0.95;q)} \tag{2.11}$$

where $L(\theta_p)$ is the likelihood of the PDF with parameter vector θ_p (which are swept), $L(\hat{\theta}_p)$ is the maximum likelihood estimate, q is the number of free parameters of the PDF and $\chi^2_{(0.95;q)}$ is the 95% percentile of the chi-square distribution with q degrees of freedom [22]. If the PDF has a single parameter, the inequation describes a curve, and if the PDF has two parameters, it defines an area.

Figure 2.6 shows the LRT curve for the POFACETs^{TM} helicopter. Because the 95% percentile of the chi-square distribution with two degrees of freedom is 5.991, the 95% confident confidence interval of the lognormal parameters is an oval with μ between 0.2 and 0.65 and σ between 1.63 and 1.93.

The sensitivity of fit is important because it allows to determine confidence intervals on the PDF parameters selection. If the interval is too wide, the uncertainty will propagate to any value computed using the RCS PDF.

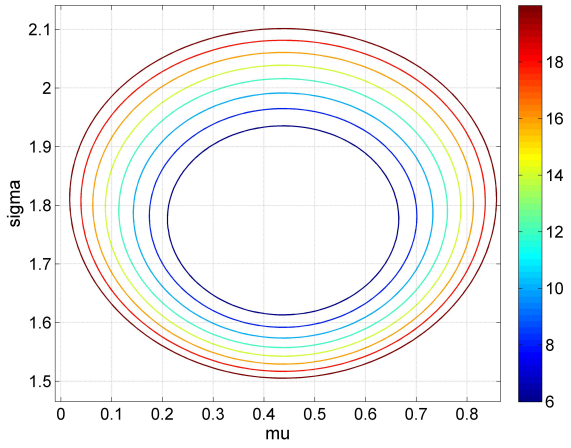

Figure 2.6: Likelihood ratio test of POFACETs^{TM} helicopter for the lognormal PDF

2.4.2 The Auto Correlation Function

Notes on Coherent Integration

Because the radar return power from a target diminishes as a function of the fourth square root of the range, the SNR in the radar receiver tends to be low. To increase the SNR, it is common to integrate (average) radar return samples [13]. If the integration occurs before detection, it is called coherent integration.

The fundamental principle of coherent integration is that the average noise voltage will tend toward zero but the target echoes will add up constructively to form a stronger echo. Figure 2.7 shows a possible integration strategy. A range gate is defined as a complex sample of the radar return. Although the number of pulses and range gates are arbitrarily set to three in the figure, the concepts extend to different numbers. For a high range resolution RCS measurement radar, the final value of Figure 2.7 would be the uncalibrated RCS estimation of the target when it spans multiple range bins.

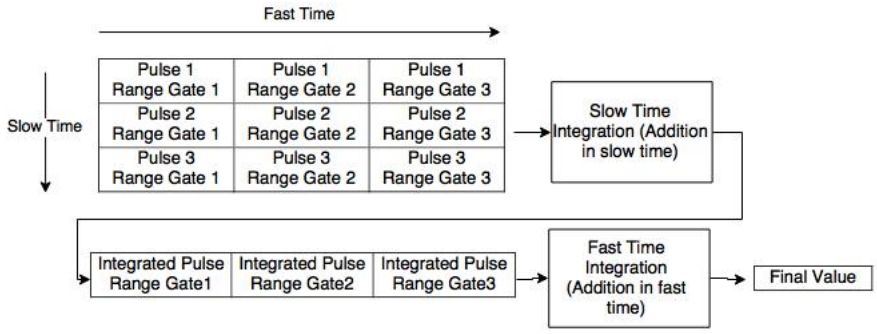

Figure 2.7: Coherent Integration

Coherent integration only works if the target echoes add coherently. This only happens if the return phase does not change considerably while pulses are integrated. However, the PDF of the RCS, alone, does not give any indication of how fast the RCS phase changes over time as the UAV moves.

An Approximation to the ACF

Although the PDF allows one to estimate the probability that the target exhibits a certain RCS value at a given sample, it must be complemented by the Auto Correlation Function (ACF) to determine how many pulses the radar can integrate coherently. The maximum integration time is called the Coher-

ent Pulse Interval (CPI) [13]. Decorrelation of the RCS may be induced by changes in range, aspect angle and frequency. Although the CPI varies drastically from target-to-target, reference [13] shows the computation to determine the change in aspect angle or frequency required to decorrelate the returns of a uniform line of scatterers. It is assumed that the decorrelation angle corresponds to the first zero of the autocorrelation function. The decorrelation angle, in radians, is given by:

$$\Delta\phi_{decor} = \frac{\lambda}{2L_{scat}} \tag{2.12}$$

where L_{scat} is the length of the scatterers line array in meters.

Using this equation as a first order approximation, the POFACETs^{TM} helicopter with a length of 6 m has a decorrelation angle of 0.0025 rad at 10 GHz. Conversely, the time required for the helicopter echoes to become decorrelated is the amount of time it takes for the aspect angle to change by $\Delta\phi_{decor}$ [13]. For the same helicopter flying at 100 km/h perpendicular to the radar at a range of 1 km, pulses can be integrated for 90 milliseconds. This time lapse allows significant integration at medium and high pulse repetition frequencies (above 10 kHz) and increases with range.

The PDF and ACF are combined to form the target fluctuation model. Both functions are necessary to compute the static probabilities of detection. The computation of probabilities of detection will be discussed in Section 2.6. The ACF will only be used in this thesis to ensure that the RCS is constant during the integration time of the measurement radar.

2.5 Dynamic Radar Cross-Section Measurements

A moving or hovering target will suffer from vibration and deformation. The Doppler effects and modulation caused by rotating propellers or engine parts will occur as well. Because of these variations, the UAV's RCS will not be deterministic for a given aspect angle: it is random and will vary depending on the flight profile, shape, position of the propellers, etc [9]. During the static RCS measurement process, the target was only allowed to move in three degrees of freedom (yaw, pitch, roll). Dynamic RCS measurements are taken while the target is also moving in the x,y and z directions or hovering. Detection theory predicts the probabilities of detection of any target most accurately when dynamic RCS values are used for the calculation [9]. Using static RCS values will result in inaccurate probability of detection, especially for very high and very low signal to noise ratios [9].

Dynamic RCS measurements are made on a range with a radar tracking the target as it moves [9]. The radar is initially calibrated with the return of an object of known RCS σ_{cal} that is usually towed or dropped. The calibrated dynamic RCS of the target σ_{target} is given by:

$$\sigma_{target} = \frac{P_{target}\sigma_{cal}}{P_{cal}} \left(\frac{R_{target}}{R_{cal}} \right)^4 \tag{2.13}$$

where P_{target} and P_{cal} are the power received when measuring the target and calibration object and R_{target} and R_{cal} are the ranges. This is a comparative method of calibration.

After calibration, the target maintains a flight profile while recording its exact location and attitude using on-board electronics. On the ground, the radar records the amplitude and time of each returned pulse. Finally, both data sets are merged together to determine the RCS versus aspect angle.

Dynamic RCS measurement campaigns generate a substantial amount of data that needs to be processed. The most common approach is to sort the data in aspect yaw and pitch bins [9]. After enough RCS values have been measured for a bin, it is possible to estimate the PDF of that bin. Reference [9] suggests at least 100 measurements must be taken by bin, but does not justify that number. This PDF will be used to calculate the probability of a radar detecting the target at that aspect angle. This is different from the static RCS where a single PDF is computed for the UAV. If the target is to maintain a given trajectory that spans multiple aspect angle bins, the data can be grouped together with surrounding bins to determine a combined PDF. A practical example is the calculation of an air vehicle penetration range. For that purpose, bins from the aspect angles around the nose are used to generate the PDF.

No literature was found regarding how the bins should be combined for a full-UAV PDF, especially considering that bins may have different numbers of measurements within them. Furthermore, no literature was found on the recommended width of the bins. However, it is common practice for RCS specialists to average contiguous static RCS values to reduce the data set to a few meaningful results. For example, RCS measurements between 0 and 10 degrees in yaw may be averaged to give a single RCS value. Angle width of 1 to 10 degrees are typically used [23]. This practice is similar to the grouping in bins during dynamic measurements, and as such, a bin width of ten degrees will be used during this thesis.

2.5.1 Dealing with Below Detection Limit Measurements

A problem encountered in the dynamic measurement of RCS is that the equipment may not be sensitive enough to measure the RCS of the target for all possible ranges. For aspect angles with very low RCS or at great ranges, measurement noise or clutter may mask the target return. Such a condition is called left-censoring and is the result of a low signal-to-clutter and noise ratio (SCNR). A possible way to deal with the issue is to store left-censored values. Left-censoring implies that some measurements are saved as equal or less than a limit. For example, one might know that a specific RCS measurement is lower than 10 dBsm, but not know the precise value. As a result, sample statistics (mean, variance, percentiles) are not defined. This technique will be used later in Chapter 5.

To determine the PDF within a bin that contains censored measurements, equation (2.9) must be modified to account for censorship. The likelihood function becomes:

$$L(\theta_p) = \prod_{i=1}^{n} F(\sigma_i;\theta_p)^{1-\delta_i} p(\sigma_i;\theta_p)^{\delta_i} \tag{2.14}$$

where θ_p is the vector of parameters of the PDF, n is the number of measurements, $F(\sigma_i;\theta_p)$ and $p(\sigma_i;\theta_p)$ are the cumulative distribution function (CDF) and PDF and δ_i is 0 for a censored measurement, and 1 otherwise [22]. In the case of a censored measurement, the value of the CDF is maximized because the RCS is known to be less than the measured RCS. When the measurement is not censored, the PDF is maximized as in Equation (2.9). The maximum likelihood estimate can then be used to select a PDF based on the Akaike Information Criterion of Equation (2.10).

Once a PDF is selected, it may be useful to determine its mean to plot it against the yaw aspect angle. Whereas the static RCS was deterministic, the dynamic RCS is a random variable and a confidence interval of the mean may be computed. Computing confidence intervals for censored data requires different techniques than for uncensored data because the sample mean and variances are not defined in the traditional sense. El-Shaarawi derived an approximation to the confidence interval of the lognormal mean in [24]. The 95% confidence upper bound is approximately:

$$\eta < \hat{\eta} \exp\left(1.96\sqrt{Var(\hat{\mu}) + 2\hat{\sigma}Cov(\hat{\mu},\hat{\sigma}) + Var(\hat{\sigma})\hat{\sigma}^2}\right) \tag{2.15}$$

where η is the true mean of the population, $\hat{\eta}$ is the mean of the PDF and $\hat{\mu}$ and $\hat{\sigma}$ are the scale and location parameters of the lognormal PDF fitted

using the maximum likelihood method. El-Shaarawi conducted simulated experiments in [24] showing the confidence interval to give intuitive results: the interval narrows as the number of measurement increases and the proportion of censored measurements diminishes. Only the lognormal case is investigated because the results of Section 5.3.1 will show that the RCS of the AR.Drone is well modeled by a lognormal PDF.

2.6 Calculation of Probability of Detection

Once the most likely PDF representing the RCS of the target has been selected, it may be used to compute the probability of a specific radar detecting that target at a given range in white noise. The generic method is described in [25] and is summarized below.

The probability of detecting (PoD) a target depends on the amount of energy reflected back towards the receiver, on the amount of noise in the receiver and on the probability of false alarm that can be tolerated. The first step is to find the probability of detection as a function of the average SNR $\bar{x}$.

The probability of detection is given by:

$$PoD(\bar{x}) = \int_0^\infty Q(\sqrt{2x}, \sqrt{-2\ln(P_{FA})})p(x;\bar{x})dx \tag{2.16}$$

where Q is the Marcum Q function, P_{FA} is the probability of false alarm and $p(x;\bar{x})$ is the conditional PDF of the received signal power in the receiver that depends on $\bar{x}$ [25]. The PDF $p(x;\bar{x})$ is based on the PDF of the target's RCS, but at different SNRs. For a lognormal target model, the integration must be done numerically [25]. Figure 2.8 shows the probability of detecting the POFACETs$^{\text{TM}}$ helicopter based on a fitted lognormal PDF.

Once $PoD(\bar{x})$ is found, the detection range can be found by converting the average SNR $\bar{x}$ to a range using the radar range equation. To do so, the noise power in the receiver must be known, along with all parameters of the radar range equation. The range is given by:

$$R = \sqrt[4]{\frac{P_t G^2 \lambda^2 \sigma_{mean}}{\bar{x} P_{noise} (4\pi)^3}} \tag{2.17}$$

where P_{noise} is the power of the noise and σ_{mean} is the mean of the RCS PDF of the target [12]. Figure 2.9 shows the POFACETs$^{\text{TM}}$ helicopter probability of detection versus the range for a transmitted power of 1 W, a gain of 27 dB, a wavelength of 0.0375 m and a noise power of 3 μW.

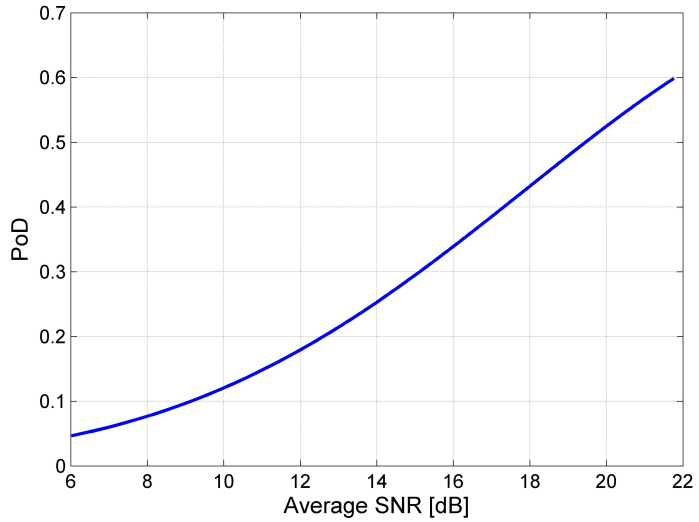

Figure 2.8: Probability of detection (PoD) of POFACETs^{TM} helicopter versus average SNR

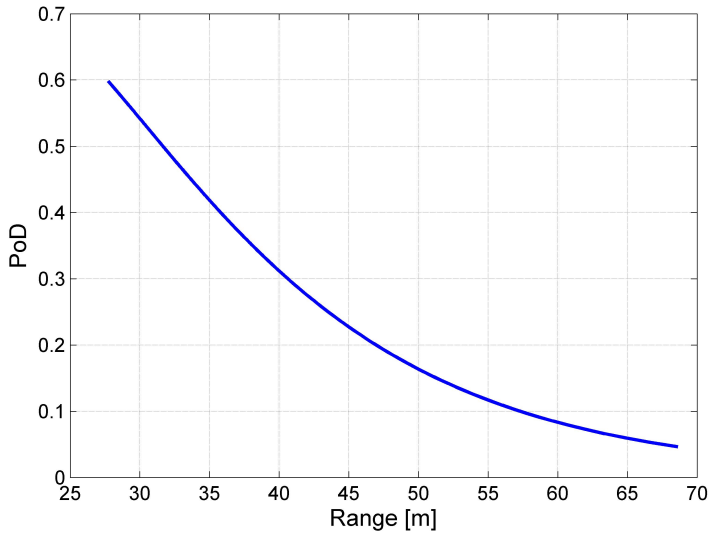

Figure 2.9: Probability of detection of POFACETs^{TM} helicopter versus range

The probability of detection is an operationally-relevant radar performance metric that can be used to optimize the radar configuration. Different probability of detection curves may be traced for various radar frequencies and polarization, and the configuration that increases the detection range for a given probability of detection is chosen.

2.7 Summary

A review of various RCS measurement methods was provided. Computer simulations may be performed by using full-wave or high-frequency asymptotic methods. Although full-wave methods are preferred as they compute an exact solution to Maxwell's equations, high-frequency asymptotic methods may be necessary to reduce the simulation time and memory requirements. Anechoic chamber measurements may be required to obtain more realistic RCS values or to validate simulation results.

Dynamic RCS measurements are taken in a range while the target is in motion. The radar return and positional data are merged together to compute the RCS of the target against the illumination angle and compensate for range attenuation. The advantage of dynamic measurement is that target vibrations, deformations and moving parts are accounted for, making the results more operationally relevant.

Notwithstanding how the RCS data was obtained, statistical characterization allows to compute the target RCS PDF. In turn, the PDF can be used to compute probabilities of detection of the target by a known radar.

3 Conventional Static RCS Measurement Techniques

This chapter presents the results obtained by simulating and measuring the static RCS of the AR.Drone using conventional methods. Section 3.1 describes the physical dimensions and properties of the UAV, Section 3.2 shows the results from computer simulations, and Section 3.3 describes the measurement setup in the Royal Military College of Canada (RMCC) Anechoic Chamber and presents the results.

3.1 The Parrot AR.Drone

The AR.Drone [26] is a quadcopter built by Parrot^{TM} and is shown in Figure 3.1. It is chosen as a test drone due to its low retail price that makes it a popular choice amongst hobbyists: the quadcopter that crashed at the German Chancellor's feet in 2013 was an AR.Drone [3].

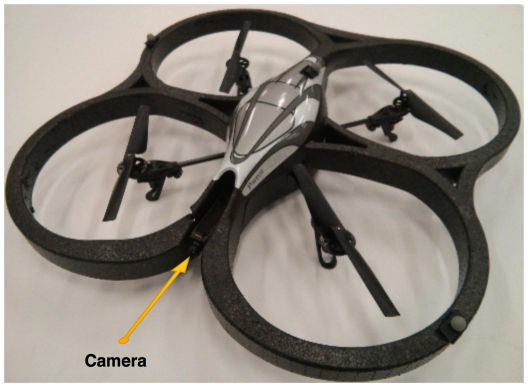

Figure 3.1: The Parrot^{TM} AR.Drone

Figure 3.2 shows a computer model of the AR.Drone acquired from [27] and defines the yaw and pitch angles that will be used to present the results. The drone has a length L of 51.7 centimeter (cm) and a width W of 45.1 cm. The front-facing camera, propellers and internal circuitry are protected by a foam case. The drone movement is controlled via WiFi using the AR.Freeflight application installed on a mobile device [26].

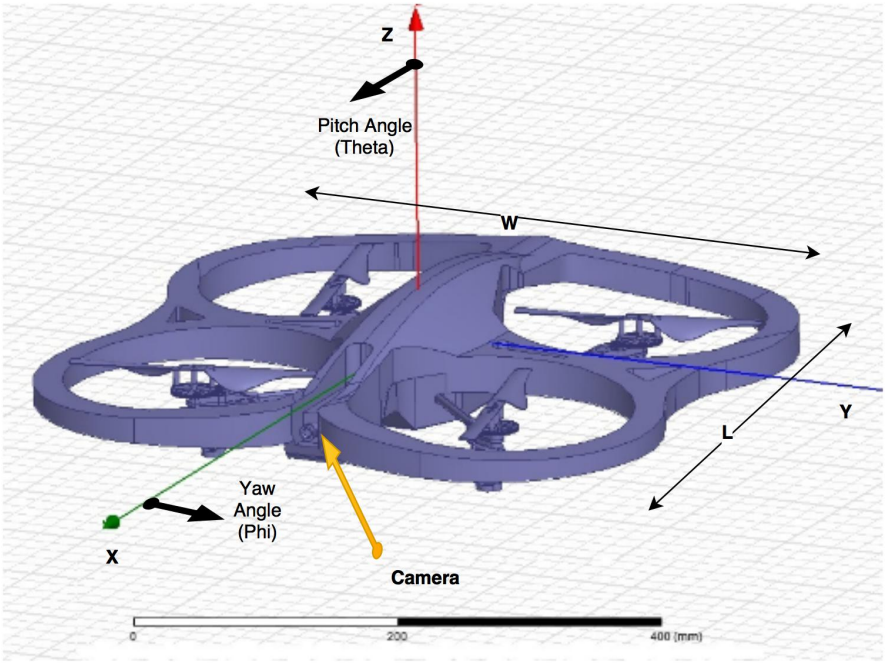

Figure 3.2: The Parrot^{TM} AR.Drone axis definition

The AR.Drone used during the measurement campaigns has a modified power system. The original battery is replaced by a Rotor RC Extreme Power battery [28]. Due to the different sizes, the Rotor RC battery is placed on top of the AR.Drone battery compartment as shown in Figure 3.3. The new battery is secured using straps. Of importance is that the exact positioning of the battery and its wires will vary during flight time, and between battery replacements. Depending on the charge and overall condition ("health") of the battery, flight time averages five minutes.

Figure 3.3: The AR.Drone modified battery holder (foam removed for illustration purposes)

3.2 Computer Simulations

The simulation of the AR.Drone required a 3D model of the UAV. The model was acquired from the GrabCAD^{TM} website (see ref [27]). The Electromagnetic Simulation Software HFSS^{TM} was used to perform the simulation [29].

The model from [27] is too detailed to run using the HFSS Finite-Element solver (see Section 2.2). The simulation failed after filling the computer's 16 gigabytes of random access memory. In order to simplify the simulation, parts of the model were removed. Figure 3.4 shows what was left of the drone after this simplification. The exterior shell of the AR.Drone was modeled by using polystyrene and the front-facing camera was replaced by a PEC plate. The engines were modeled using PEC as well and the electronics (circuit board, wiring, etc) were simplified by using a PEC polyhedron. Finally, the propellers, gears, screws, styrofoam casings and plastic parts were all removed from the model because their contribution to the RCS was assumed to be negligible when compared to the modeled parts. The validity of this assumption will be investigated in Section 3.3 by measuring the RCS in an anechoic chamber.

The simulation was run using the HFSS physical optics solver (see Section 2.2) instead of the FEM solver and the results are shown in Figure 3.5 for a pitch angle (θ) of 90 degrees and an angular resolution $\Delta\phi_{res}$ of 1 degree. The RCS of the UAV varies significantly between -15 dBsm and -46 dBsm depending on the yaw angle. The simulation required a peak volatile memory allocation of 4.51 GB and 7 hours to complete.

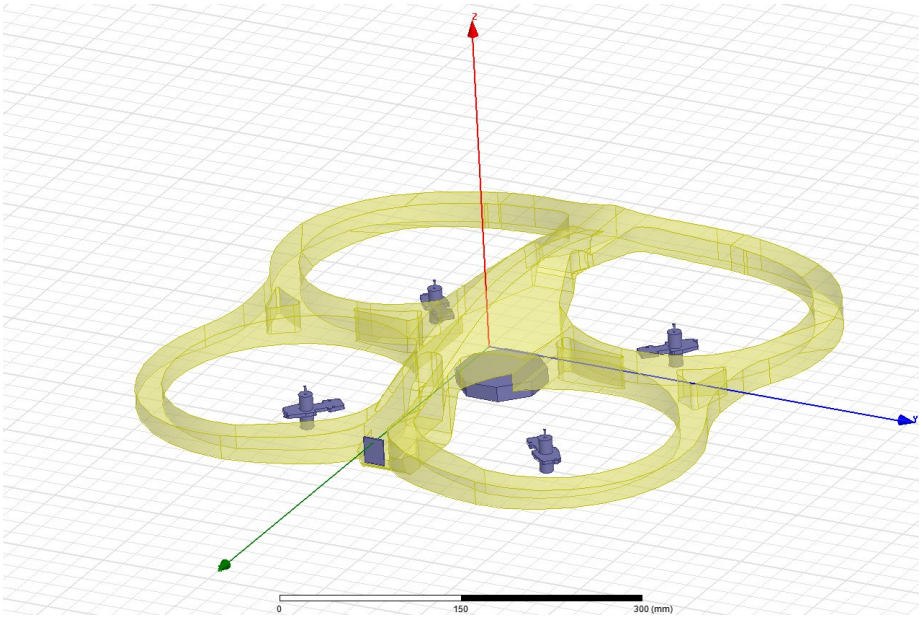

Figure 3.4: Simplified AR.Drone model

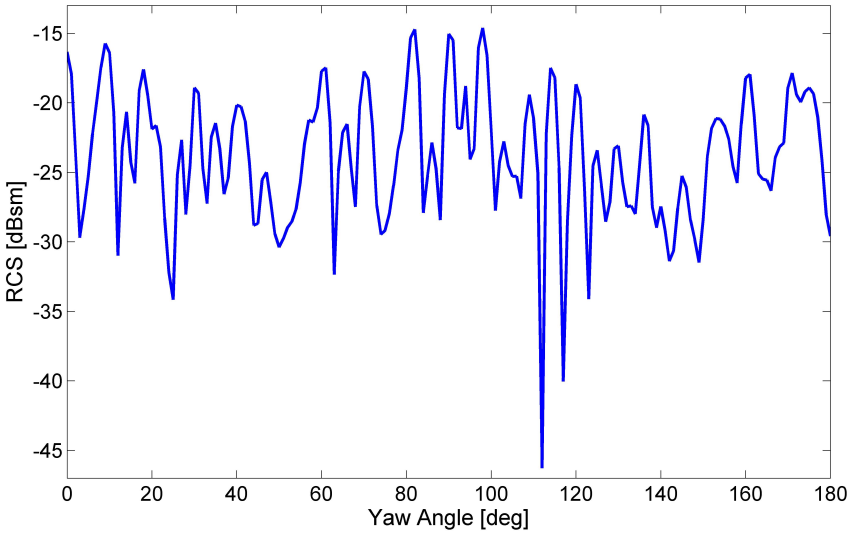

Figure 3.5: Static RCS simulation at 8 GHz VV

3.3 Anechoic Chamber Measurements

The RMCC's anechoic chamber was used to perform static RCS measurements in the frequency domain. The measurement methodology was based on Section 2.3. The transmit and receive antennas were placed 5.08 m from the target pedestal. The angular offset between the center of the pedestal and each antenna is 1.58 degrees, which is small enough to make the quasi-monostatic approximation [11]. The Agilent^{TM} Performance Network Analyzer PNA-X N5244A was used to measure the continuous wave (CW) stepped frequency signal. The transmitter swept from 5 to 11 GHz and a stepped frequency sweep was selected, with a dwell time of 1 μs to allow for the local oscillator to settle. To reduce the noise power, the IF bandwidth was set to 10 kHz. With an averaging factor of 256 and by taking 401 measurements per sweep, the single sweep time was maintained below 13 seconds, thereby reaching a compromise between measurement time and sensitivity.

The calibration was performed using the built-in RCS calibration routine. A 12-inch diameter metallic sphere was used as a calibration object, and the results were verified using a 8-inch sphere. Figure 3.6 shows the theoretical RCS of the 8-inch diameter sphere versus the measurements. The difference between both RCS curves may be explained by multi-path effects between the sphere and the pedestal. Diffraction at the edge of the RMCC anechoic chamber pedestal was observed in [11] and the error levels are consistent with the error observed in Figure 3.6, with a maximum error of less than 1 dB at a level of -15 dBsm.

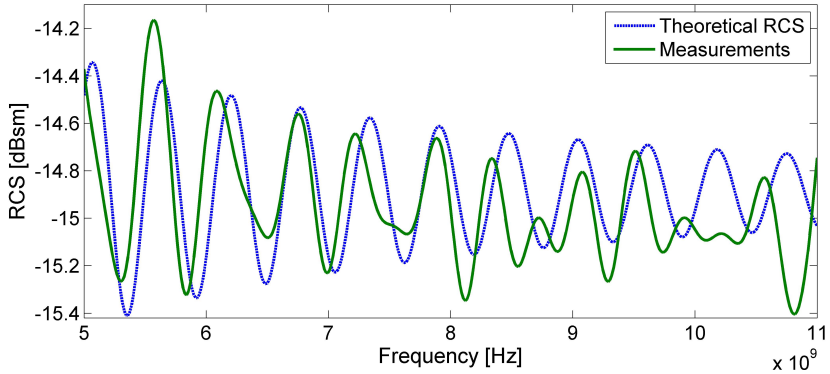

Figure 3.6: Anechoic chamber calibration verification using an 8-inch diameter sphere

The AR.Drone was then placed on the target pedestal and its RCS is measured against the yaw angle ϕ. Because of the UAV's assumed symmetry about the x axis, ϕ was only varied from 0 to 180 degrees. This symmetry will be used for the remainder of this thesis. Measurements at different pitch angles θ were taken by increasing the height of the target pedestal. Each set of measurements with a constant pitch angle θ is referred to as a slice. Figure 3.7 shows the VV RCS versus the yaw aspect angle for pitch angles θ of 90, 89.4 and 88.8 degrees. These angles were chosen because the target pedestal can only be raised by increments of 5.5 cm.

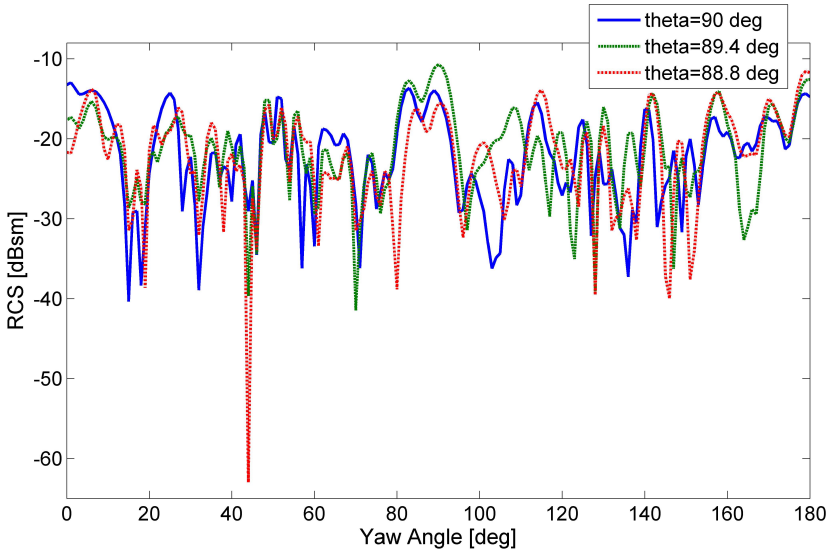

Figure 3.7: Static VV RCS measurements at 8 GHz

The impact of the number of slices measured can best be illustrated by computing its effect on the selected PDF. Figure 3.8 shows the PDF fitted on the RCS measurements for the single broadside ($\theta = 90\,\text{deg}$) slice and the amalgamation of the three slices at 8 GHz. Even if the pitch angle may have a significant impact on the RCS for a given yaw angle, the effect of the amalgamation of these three slices is very small on the PDF when compared with the single broadside slice. This may be explained by the fact that the number of sharp nulls and peaks is very consistent for the various pitch angles close to 90 degrees, even if they appear at different yaw angles. Based on these results, only the broadside slice will be measured or computed for the remainder of this thesis.

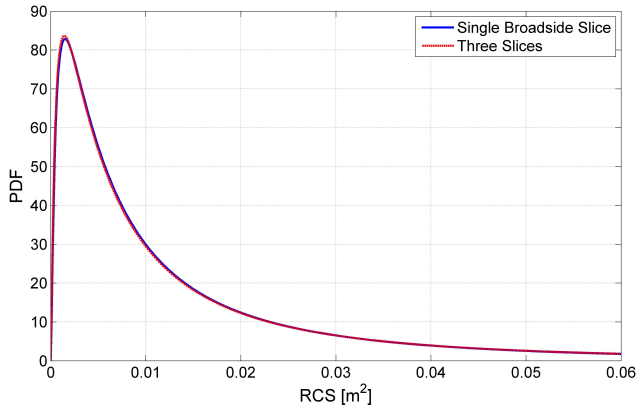

Figure 3.8: Impact of pitch angle illumination on PDF

3.3.1 Comparison with the Simulated RCS

The measured RCS shown in Figure 3.7 is different than the simulated RCS in Figure 3.5. The difference may be explained by: the use of a high-frequency asymptotic method in simulation, the simplification of the AR.Drone model to reduce simulation time and memory usage, and the uncertainty of the material parameters used for the different UAV parts.

The fitted PDFs for simulated and measured RCS at 8 GHz using a VV polarization are shown in Figure 3.9. The overall marked difference between both PDFs may be quantified by the 3 dB difference between their mean.

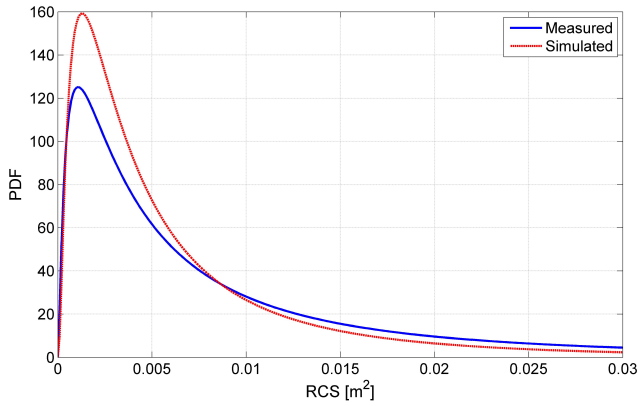

Figure 3.9: Simulated and measured RCS PDFs

Based on the results of Figure 3.9, measurements are considered superior to simulated results and will be used for the reminder of this thesis. Nevertheless, simulation may provide an acceptable estimate of the RCS depending on the application.

3.3.2 Notes on Angular Sampling Resolution

A factor affecting the accuracy of static RCS measurements is the yaw angular resolution. To determine its impact on the AR.Drone, the RCS (amplitude and phase) for yaw angles between 0 and 70 degrees is measured at a resolution $\Delta\phi_{res}$ of 0.1 degree.

Figure 3.10 shows the frequency domain of the RCS angular signal at 8 GHz. As shown on the graph, the strength of the normalized FFT is -15.93 dB at -0.5 deg^{-1} and -16.91 dB at 0.5 deg^{-1}. Therefore, by selecting an angular resolution of one degree, which results in a Nyquist frequency of 0.5 deg^{-1}, aliasing should not affect the data significantly. An angular resolution of 1/6th of a degree would almost remove aliasing completely,but would increase the measurement time to an impractical duration. Based on those results, an angular resolution $\Delta\phi_{res}$ of 1 degree is used for this thesis when taking static measurements.

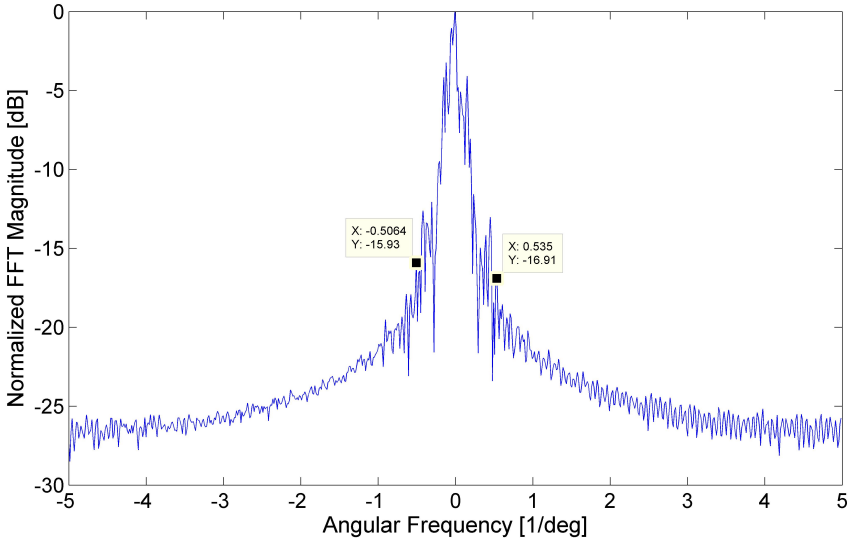

Figure 3.10: Frequency domain of 8 GHz RCS measurement signal in anechoic chamber

3.3.3 Inverse SAR Imaging

The static measurements in the anechoic chamber may be used to generate a two-dimensional ISAR image. Section 2.3.1 describes the image formation process. The ISAR images will be used to determine the minimum range to satisfy the far-field requirement in Section 5.1.3. Furthermore, they will provide some insight as to the scattering mechanisms.

To validate the image formation algorithm of Section 2.3.1, a cylindrical and a semi-circular target are placed on the foam pedestal of the anechoic chamber, as shown in Figure 3.11. The 30-cm ruler is shown to better illustrate the distances on the image and is removed during measurements. Both targets are separated by 20 cm in range and 25 cm in cross-range.

Figure 3.11: Test case ISAR setup

The targets are rotated by 21 degrees to give a cross-range resolution of 5 cm. The anechoic chamber transmitter sweeps from 5 GHz to 11 GHz for a range resolution of 4.88 cm. Figure 3.12 shows the inverse SAR radar image. Both targets are clearly visible and separated by the correct distance.

The AR.Drone is placed on the target pedestal with the camera facing the anechoic chamber transmitter ($\phi = 0$). The same rotation is applied as for the test case, resulting in the radar image of Figure 3.13. Clearly visible on the image are the four engines, the camera and the body of the AR.Drone. The most reflective part of the drone is the body with a peak distributed RCS of -23.5 dBsm, followed by the camera at -26 dBsm. The return of the engines is 5 dB below the return of the body. As such, most of the return is confined within 10 cm in yaw.

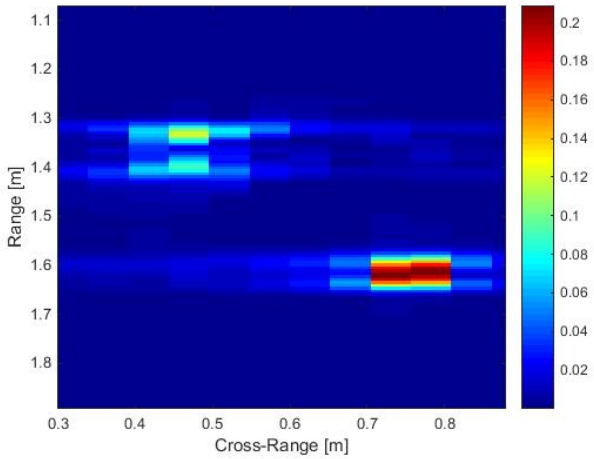

Figure 3.12: Test case ISAR image

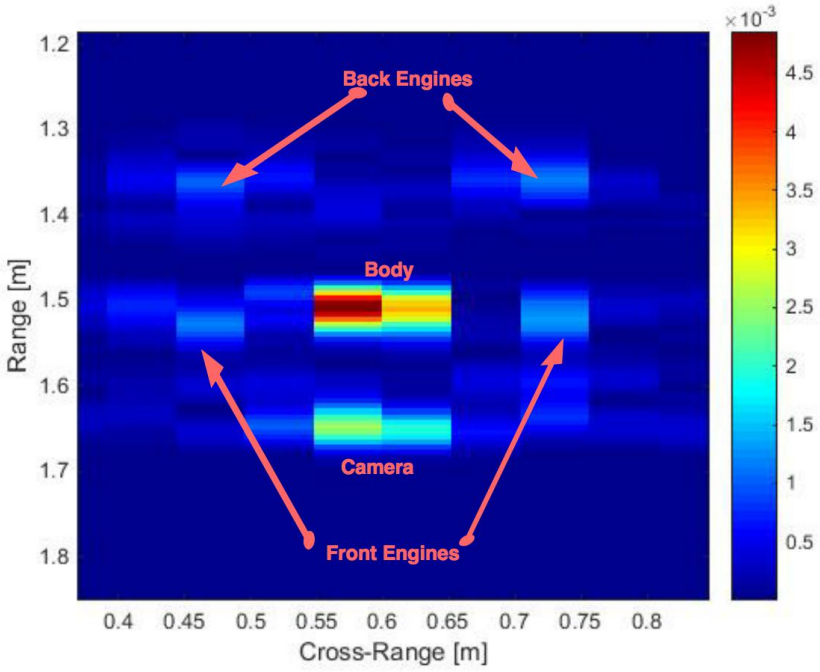

Figure 3.13: ISAR image of the front of the AR.Drone

The AR.Drone is then rotated 90 degrees so that its broadside faces the transmitter ($\phi = 90\,\text{deg}$). Figure 3.14 shows the resulting radar image. Most of the radar return is confined within twenty cm in yaw. The front engines are barely discernible on the image because their RCS is very small at that specific aspect angle. To confirm this result, the RCS of the front left engine is measured in isolation in the anechoic chamber after having been removed from the AR.Drone. Its RCS is measured at -27 dBsm when facing the radar in the same position as in Figure 3.13 and -33 dBsm when it is in the same position as Figure 3.14. The results are therefore consistent with the ISAR images. Both ISAR images will be used in Chapter 5 to determine the minimum range between the radar and the drone to satisfy the far-field requirement.

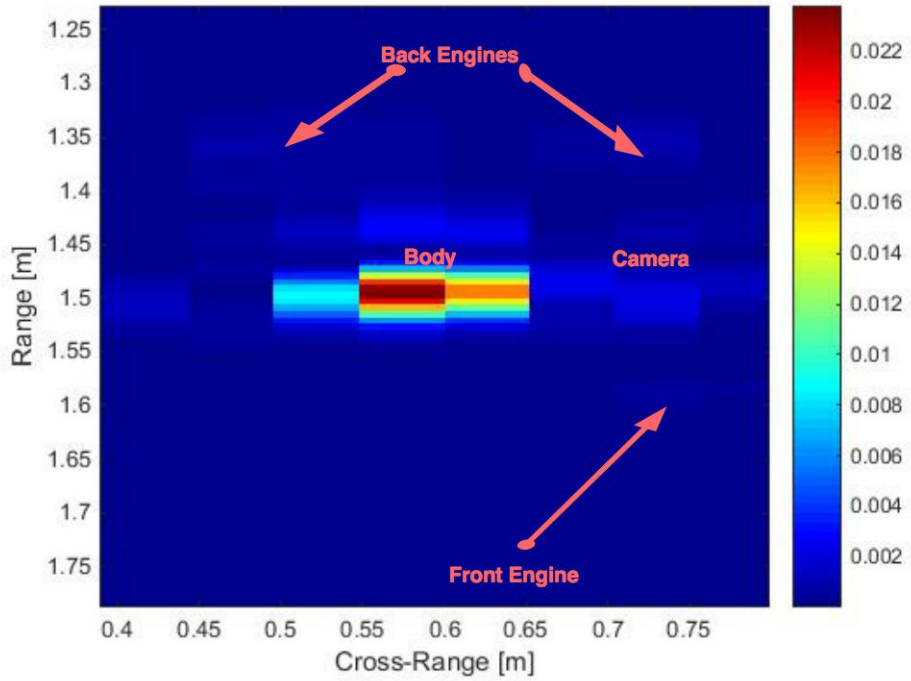

Figure 3.14: ISAR image of the side of the AR.Drone

3.4 Summary

Conventional methods may be used to determine the static RCS of a target. The first method, computer simulation, provides an approximation of the RCS for which the accuracy depends on the accuracy of the model and the chosen numerical method. The geometry and materials must be modeled with great care. By using high-frequency asymptotic methods and by reducing the complexity of the model, a first-order approximation of the RCS of the AR.Drone is obtained (Figure 3.5).

The second method investigated consists in measuring the RCS of the AR.Drone in an anechoic chamber. The results of Figure 3.7 differ from the simulated RCS and both methods yield different PDF. Given the choice, one should always choose measurement over simulation given that simulations require significant simplifications to accommodate computer speed and memory limitations. Finally, ISAR imaging was used to investigate the scattering mechanisms of the UAV. The results of Figure 3.13 and 3.14 show that the most reflective part of the AR.Drone is its core.

4 The Dynamic RCS Measurement System

Conventional RCS Measurement techniques measure the target RCS while it is at rest. Although the results are precise and repeatable, there are no guarantees that they accurately represent the RCS of the target in flight. To determine the RCS of a drone in an operational environment, it must be measured dynamically.

Measuring the dynamic RCS requires some way of tracking the target whilst its RCS is being measured by the radar. Furthermore, the target attitude (aspect) must also be known so that the RCS is recorded against the illumination angles ϕ and θ. A radar and a positioning system are therefore necessary.

Typical dynamic measurement ranges are located outdoors due to the need for sufficient space to fly the target. However, in the case of mini-UAVs, indoor ranges are much more convenient. Power is readily available for the equipment, drones may be flown indoors without being affected by winds, and high frequency radars are small enough to fit within a room. For these reasons, the indoor range was chosen for the Dynamic RCS Measurement System. Unfortunately, indoor ranges cannot benefit from the global positioning system (GPS) to determine the UAV position and on on-board electronic to determine its attitude so different technology must be used.

The chosen approach to measure the dynamic RCS leverages systems that are already available in the Department of Electrical and Computer Engineering. Two independent systems will be integrated, namely the LabVolt^{TM} Radar Training System (LVRTS) [30] and the Optitrack^{TM} infrared camera tracking system [31].

This chapter provides a general description of the Dynamic RCS Measurement System and its components. Whether the system is capable of measuring the RCS of the AR.Drone accurately and precisely depends on the UAV's

physical and dynamic characteristics and on the system's configuration. This analysis is reserved for Chapter 5.

4.1 System Overview

A UAV is flown by an operator and optically tracked by the Optitrack^{TM} Tracking Tools camera system, allowing for the determination of the UAV's physical location, pitch, yaw and roll. The position and attitude of the UAV are streamed in near real-time to the *Radar Processor* Matlab^{TM} program through a network connection. At the same time, the UAV is illuminated by a modified LabVolt^{TM} Radar Training System. The radar antennas are steered using a Matlab^{TM} program called *Turret Controller*. The *Turret Controller* interacts with a custom-built turret. The radar return pulses are captured from the radar using an oscilloscope, integrated (Figure 2.7) and sent to the *Radar Processor* via a network connection. The return pulse strength is then recorded and the RCS is computed. The RCS and positional information are then merged by the *Radar Processor*, allowing to associate the RCS with the illumination angles. The results are then saved for later statistical processing.

Figure 4.1 graphically shows the interactions of the different system components. All components in yellow are custom-designed and built. Components in white are configured appropriately.

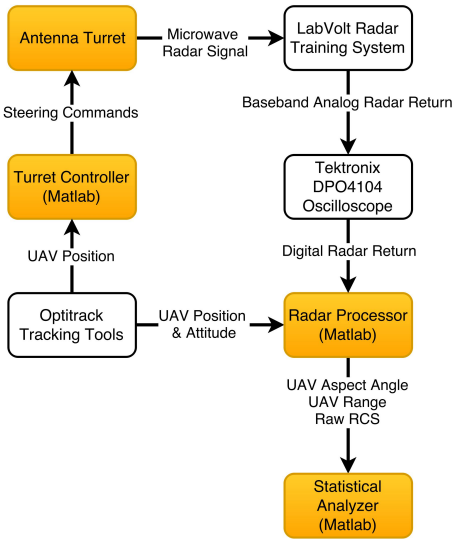

Figure 4.1: Conceptual design of the Dynamic RCS Measurement System

4.2 The Optitrack^{TM} Tracking Tools System

The Optitrack^{TM} System provides real-time position and orientation of the UAV. It is composed of 24 ceiling-mounted infrared cameras arranged in a rectangle as per the floor plan of Figure 4.2. The cameras are connected via USB to a computer running the Optitrack^{TM} Tracking Tools software [31]. The software determines the orientation and position of the UAV every 10 milliseconds and streams it in near real-time on the Ethernet network via the Natnet protocol [31].

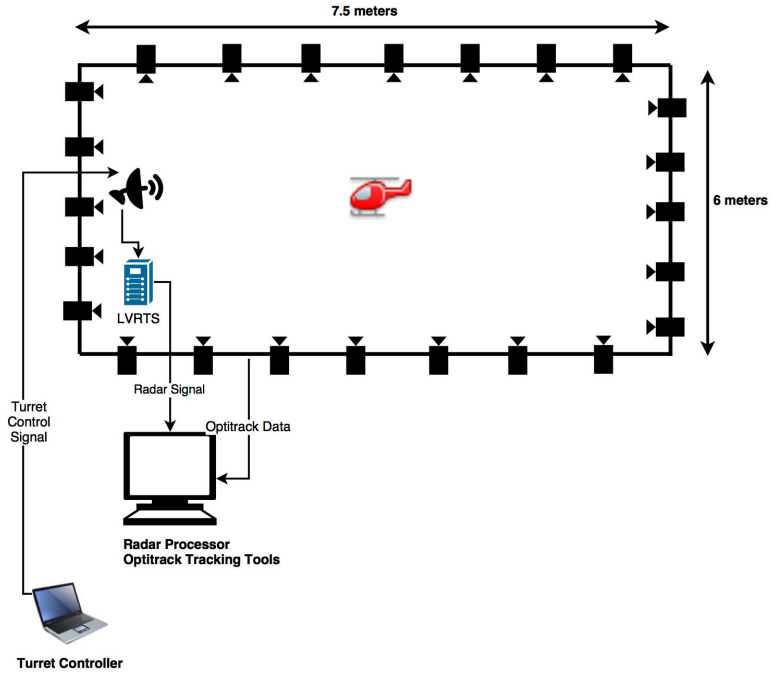

Figure 4.2: Floor plan of the Dynamic RCS Measurement System

Before data collection, three motion capture markers are placed on the UAV in a non-symmetrical fashion. The markers are detected and tracked by the software. The non-symmetry is required to ensure that the yaw, pitch and roll angles are uniquely defined. The operator then groups markers together via Tracking Tools software to form a *trackable*: the UAV. Figure 4.3 presents a screenshot of the Tracking Tools software with two trackables: the antenna turret in brown and UAV in green. The antenna turret is represented solely for the reader's situational awareness and is not necessary during system operation.

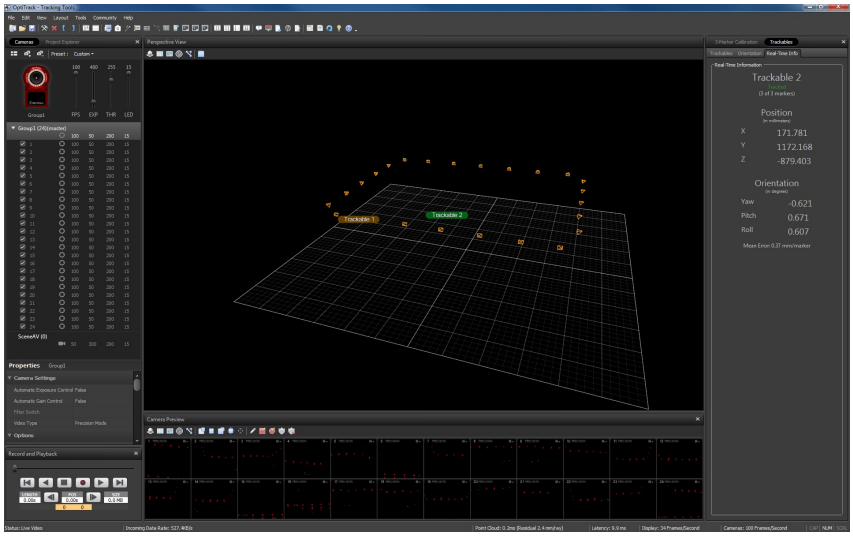

Figure 4.3: Tracking Tools Software

Tracking Tools^{TM} converts the trackable into a rigid body. The position and orientation of the rigid body are determined and streamed via the proprietary Natnet protocol. The information streamed includes the rigid body position (x, y, z) and the quaternions (qx, qy, qz, qw). New positional data is generated by the system 100 times per second with a averaged latency of 8 ms. The information is accurate within 1 cm in position and 1 degree in orientation.

Placing markers on the UAV implies that its RCS will be slightly modified. Each marker is a sphere with a diameter of 11 mm. Assuming a worst case scenario where the marker is perfectly conducting, its analytical RCS is -34.78 dBsm (3.3 cm^2) at 8 GHz. The Dynamic RCS Measurement System is therefore restricted to measuring UAVs that have an RCS greater than that value. Considering that the markers are made of plastic and not metal, this threshold is very conservative.

4.3 The Radar System

The LabVolt^{TM} Radar Training System (LVRTS) is used as the system's radar. Its transmitter is configured to output a 5 nanosecond pulse with a pulse repetition frequency of 288 Hz. The range trace length is selected as 7.2 m and the carrier frequency may be selected between 8 and 10 GHz as desired

by the operator. The coherent receiver performs time expansion [30] and the 2-channel (I and Q) received signals are sampled by a Tektronix DPO4104 oscilloscope [32]. The exact oscilloscope configuration depends on the target and is described in Section 5.1 for the AR.Drone.

The LVRTS peak transmitter output power is typically 0.5 dBm [30]. To increase the signal-to-noise ratio, the Mini-Circuit^{TM} ZVE-3W-183+ high power amplifier [33] is placed between the transmitter and antenna; thereby increasing the peak transmitted power to 35.5 dBm [33]. Considering the duty factor of the LVRTS and the size of the transmitting antenna, the power density at the antenna aperture is 1.36 W/m^2, well below the limit of 10 W/m^2 set in Health Canada Safety Code 6 [34].

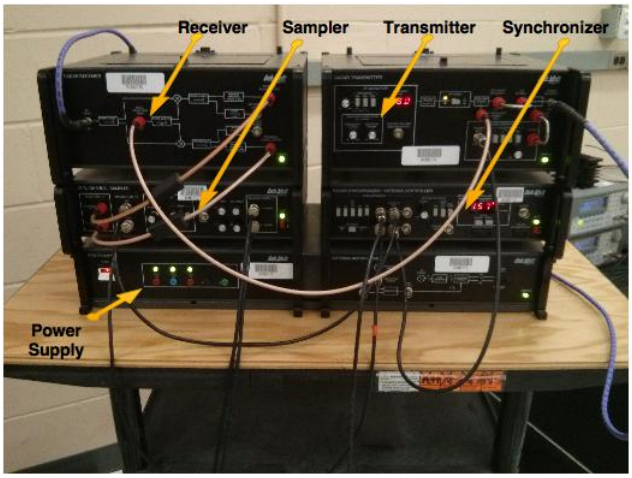

Figure 4.4: LabVolt^{TM} Radar Training System

4.4 The Custom Antenna Turret

At the core of the antenna turret is the Quanser motion testbed [28]. The turret has an azimuthal range of motion of 190 degrees, allowing it to see the whole flight area. Its elevation range is between -45 and 45 degrees. The testbed's servomotors are controlled by two Agilent Function Generators, Model 33210A [35], connected to the measurement system's Ethernet network. Each waveform generator controls either the yaw or pitch of the turret using pulse width modulated (PWM) signals. The turret includes two EMCO Model 3160-07 horn antennas [36] in a quasi-monostatic arrangement and a webcam

connected via USB to the *Turret Controller*. The antennas and webcam are mounted on a custom-designed 3D-printed structure placed on the platform of the HiQ Motion Testbed. A Vizatek model MPS-3005L [37] provide DC power for the turret servos. A picture of the turret is shown in Figure 4.5.

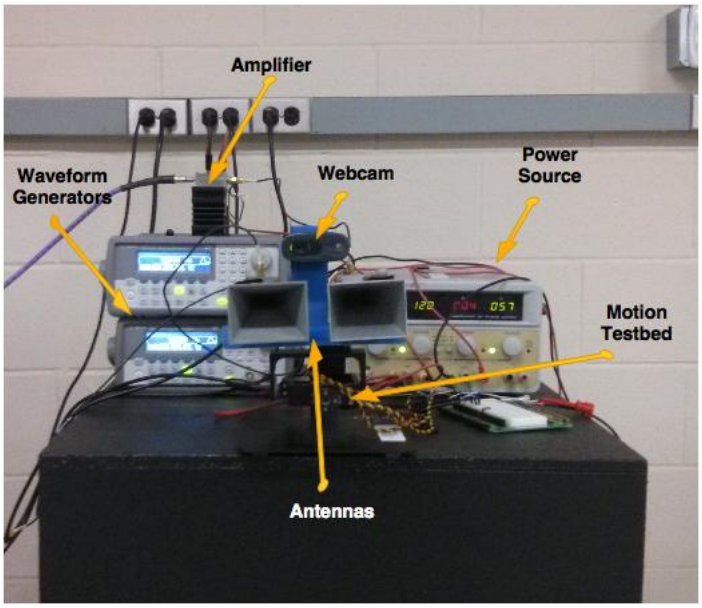

Figure 4.5: Custom antenna turret

The antenna pattern beamwidths are measured using a six-inch diameter calibration sphere. The six-inch sphere is chosen over a 12-inch diameter sphere to ease the far field requirement and over a 3-inch diameter sphere to increase the SNR. The sphere is static but the turret is rotated one degree at a time in azimuth and elevation. The results are shown in Figure 4.6. The -1 dB power beamwidths are 7 degrees in pitch and 12 degrees in yaw. The elevation pattern is less smooth than the azimuth pattern; which may be due to reflection from the ceiling. Although the multi-path reflection from the floor is removed by placing microwave absorber (see Section 4.5), it was not possible to place absorber on the ceiling due to mechanical difficulties. The suitability of the antenna patterns depends on the target size and is discussed in Chapter 5 for the AR.Drone.

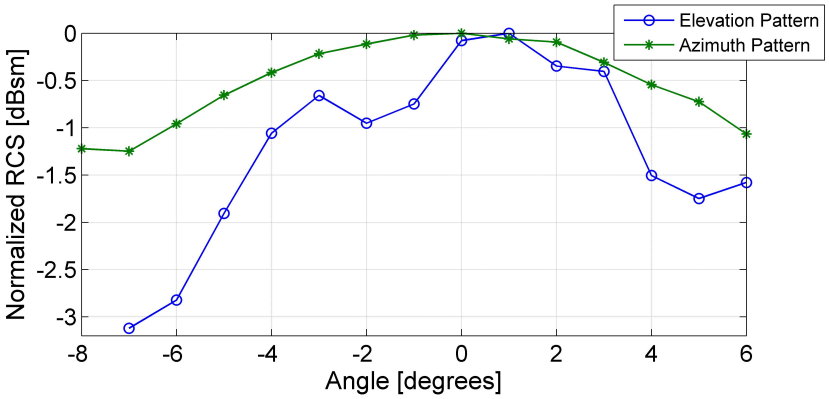

Figure 4.6: Power antenna patterns

4.5 Floor Absorber

The impact of radiated energy bouncing off of the floor and illuminating the UAV is investigated. Figure 4.7 shows the geometry of the target and radar antenna. As in [38], assume that the monostatic RCS of the direct path and the bistatic RCS of the indirect path are the same. Furthermore, from the EMCO 3060-7 antenna specifications, an antenna pattern loss of 10 dB for the indirect path is defined. The analytical RCS is expected to be [38]:

$$\sigma = \sigma_0 |1 + U\Gamma \exp(j\beta(I - D))|^4 \tag{4.1}$$

where σ_0 is the monostatic RCS, U is the antenna pattern loss at the angle towards the floor, Γ is the ground reflection coefficient, β is the wavenumber, and D and I are the direct and indirect path length respectively. Using this equation, the normalized ($\sigma_0 = 1$) measured RCS as a function of the target height is plotted, as shown in Figure 4.8 (without absorber curve).

Based on these results, it is imperative to remove the ground bounce to avoid such a high variation of the measured RCS as a function of the UAV height. To do so, the ground must be covered with absorbing material. However, because the UAV maintains a low altitude during measurements, its flight stability is affected by changes in the shape of the floor, a phenomenon known as ground effect [39]. Since the UAV may fly over the absorbing material, it is not possible to use wedged absorber. Therefore, the AN-77 flat absorber [40] is used. Based on the specifications of the AN-77 absorber, a 20 dB reduction off the signal strength reflected on the ground is expected, resulting in the normalized measured RCS of Figure 4.8 (with absorber curve).

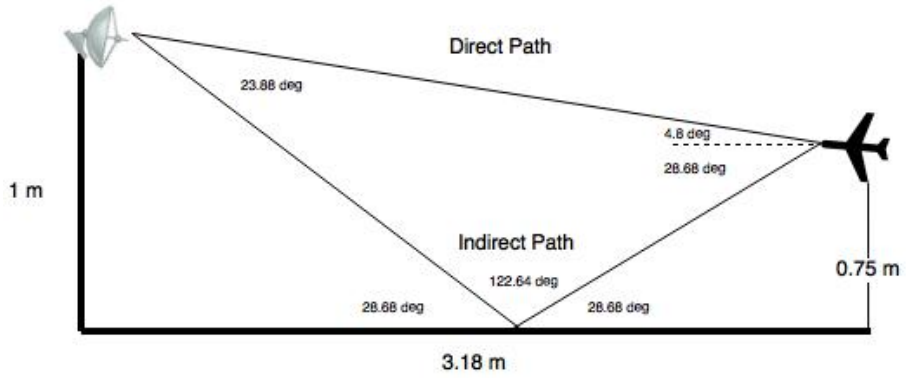

Figure 4.7: Typical ground bounce geometry

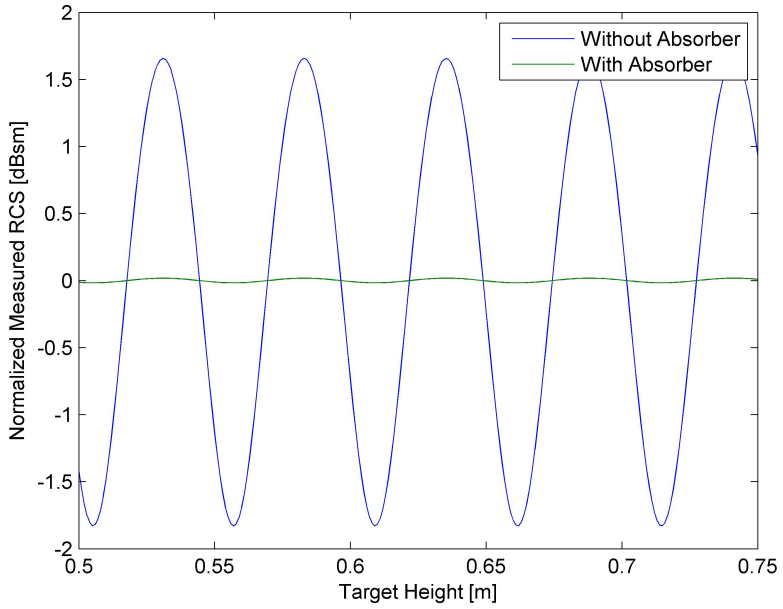

Figure 4.8: Normalized measured RCS

A variation of 0.015 dBsm based on the UAV height is deemed acceptable for the dynamic RCS measurement system.

4.6 The Turret Controller

The custom antenna turret is controlled using a Matlab program called *Turret Controller* running on a laboratory computer. The system allows for either an operator to track the UAV with a joystick while relying on the webcam image, or for the turret to track the UAV automatically with the help of the Optitrack^{TM} data. Figure 4.9 shows the automatic tracking block diagram. The algorithm is an open-loop controller that requires the operator to initially center the turret on the target, allowing the controller to determine a set of reference duty factors (DFs) against current azimuth and elevation angles. As the target moves, azimuth and elevation offsets are determined and new DFs are computed. The specifications of the Motion Testbed servomotors state that a 0.0286 change in the duty factor of the PWM input of the servos is required to change the turret orientation by one degree [41]. However, visual inspection of tracking data shows that the turret tends to under-estimate the required shift to track the UAV at this value. A value of 0.0295 visually reduces the tracking error. The effect of tracking errors on the measured RCS is investigated in Section 5.2.6.

The maximum change in duty factor is capped at a value determined by the operator. This restriction is necessary to reduce vibrations in the turret and the impact of possible errors in the Optitrack^{TM} data.

A coordination message is sent to the *Radar Processor* in order to take measurements only when the turret is centered on the target. The *Turret Controller* updates the turret position every 100 ms. It is up to the operator to select a radar integration time lower than this value so that the turret does not move during the integration time (see Section 5.1.2 for the AR.Drone). The *Turret Controller* communicates via Ethernet with the waveform function generators and the *Radar Processor* by using the Matlab Instrument Control Toolbox [42].

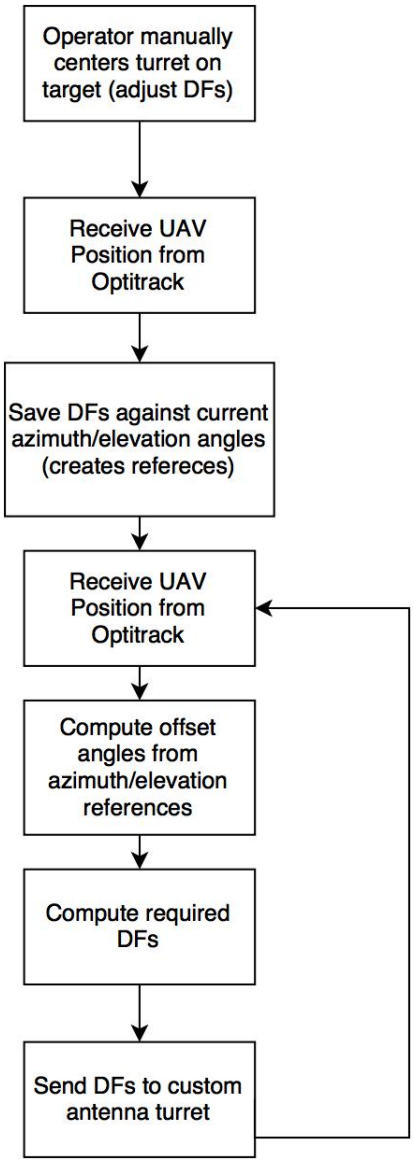

Figure 4.9: Automatic tracking algorithm

4.7 The Radar Processor

The *Radar Processor* is a Matlab^{TM} program with a custom-designed graphical user interface that collects the data from the radar and Optitrack^{TM} systems and saves it for later processing. More precisely, the *Radar Processor* saves the target attitude, the radar range, the optical range (distance between the target and radar as measured by the Optitrack^{TM} system) and the measured RCS. A screen-shot of the user interface is shown in Figure 4.10. The measurement algorithm is shown in Figure 4.11.

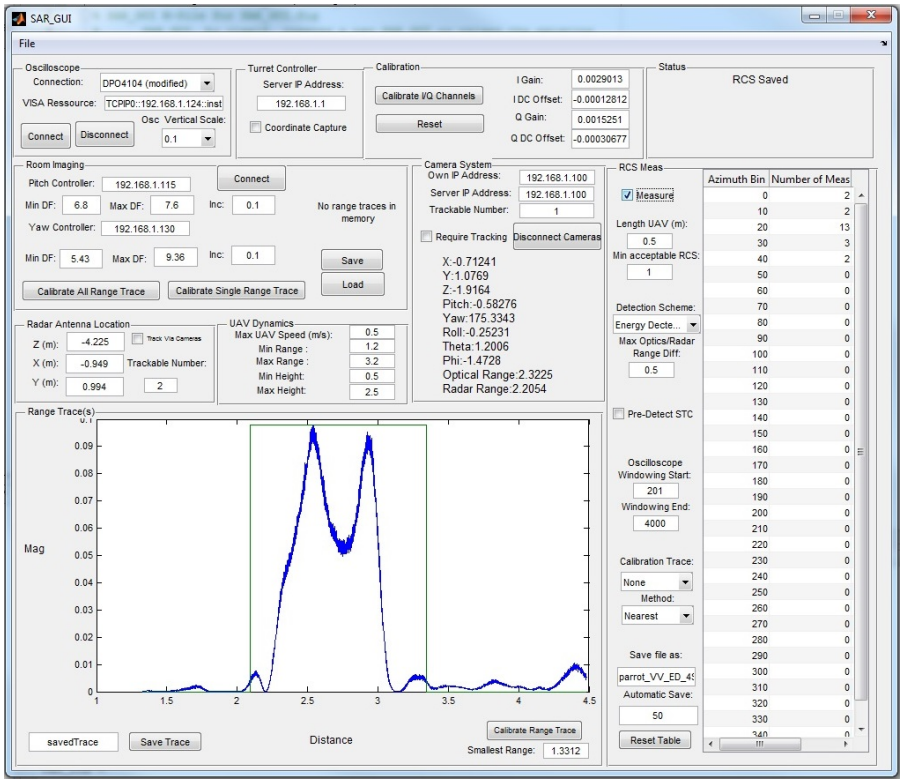

Figure 4.10: Layout of the *Radar Processor* graphical user interface

The *Radar Processor* allows the operator to specify limits on the UAV height, range and speed. Radar returns for situations falling outside of those limits are ignored. This is useful for avoiding regions of heavy clutter, but also ensures the radar integration time does not violate the UAV's ACF as given by Equation (2.12). Another advantage is that it speeds up the measurement campaign. As shown in Figure 4.11, the *Radar Processor* performs those

checks before downloading the radar return, which is the longest operation performed in the measurement cycle. It is more efficient to perform these checks during the data acquisition than in post-processing.

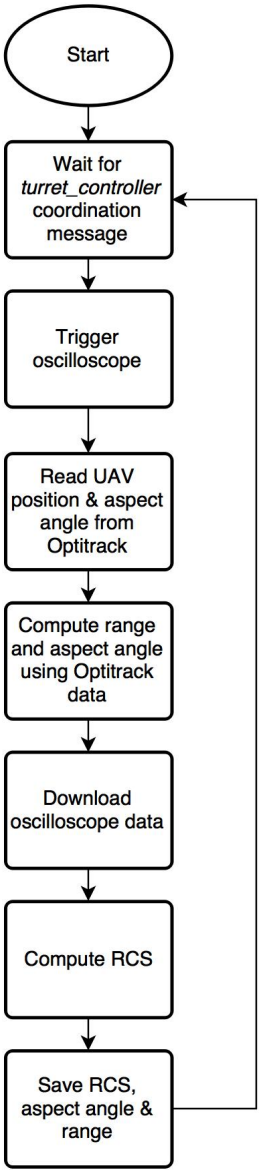

Figure 4.11: RCS measurement sequence

4.7.1 Background Subtraction

In a controlled environment like an anechoic chamber, unwanted reflections from the walls, floor and ceiling are removed by covering them with radio absorbent material (RAM). The laboratory space of Figure 4.2 is an uncontrolled environment because it is not completely covered by RAM, and unwanted reflections from the room clutter will induce an error on the measured RCS if they are not properly accounted for. A possible way to deal with unwanted reflections is to save the radar return of the empty room and to perform a vector subtraction with the radar return obtained with the target present.

The *Radar Processor* is capable of removing unwanted reflections from the room by using a background subtraction technique. The radar returns of the empty room for any user-defined turret orientations are saved in memory and a vector subtraction is performed on the radar returns measured when the target is present. For turret orientations falling in between saved empty room traces, the nearest neighbour and bilinear interpolation techniques may be used to determine the unwanted reflections to subtract to the measured radar return.

Background subtraction is not a perfect technique as it is not effective against multi-path returns [23]. The radar pulse incident on the target may bounce on it and then on the room clutter or vice-versa, before returning towards the radar receiver. These unwanted multi-path reflections are not removed by background subtraction because they did not occur when the target was not present. Furthermore, the presence of the target modifies the back-wall illumination [23]. Nevertheless, these changes to the empty-room radar return usually appear later in range than the target due to the increased travel distance of multi-path reflections. The pulse length used by the Dynamic RCS Measurement System and the size of the laboratory space allow to reduce the impact of multi-path reflections on the measured RCS by time-gating the return. The Dynamic RCS Measurement System time-gating is implemented during target detection and is explained in the following section.

4.7.2 Detection and RCS Measurement

The output of a time-domain RCS measurement depends on the pulse width. Two cases are typically considered in the literature: when the target is much smaller than the pulse width and when it is much bigger than the pulse width.

When the target is much longer than the pulse width, the target is never fully illuminated by the incident wave and a steady state (continuous-wave)

approximation is not possible. However, the improved range resolution permits the identification of different scattering centers and mechanisms, and the processing of radar images of the target. Figure 4.12 shows the time-domain return of an 8-inch diameter sphere from a radar with a 0.325 ns pulse width measured inside the RMCC anechoic chamber. The x-axis is converted from time to distance by using pulse delay ranging [12]. The radar return is split into a specular and creeping waves, as expected from the theory [13].

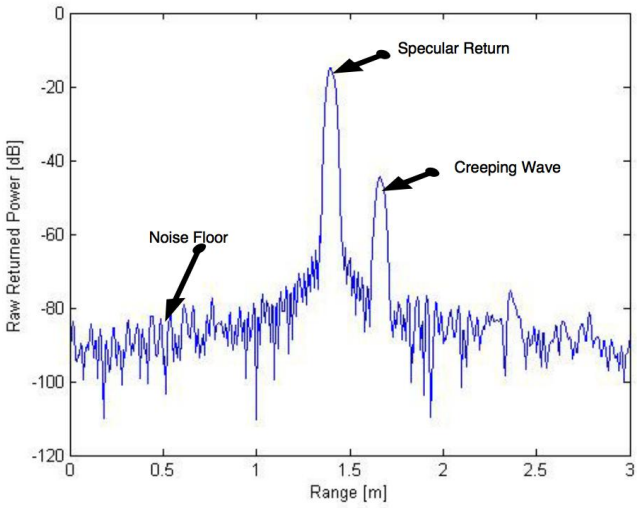

Figure 4.12: Measured radar return of 8-inch sphere (0.325 ns pulse)

Typical military search radars have a pulse width in the micro-seconds range [43], making potential targets much smaller than the pulse width. Figure 4.13 shows the time-domain return of a 6-inch diameter sphere when illuminated by a radar with a 5 nanoseconds pulse. Because the pulse width is significantly longer than the target length, the returned power stabilizes at a constant value once the target is fully illuminated and induced currents reach steady state, making a continuous-wave approximation possible. To compute the RCS, the returned signal is sampled once the target is fully illuminated [44]. The smaller the object is when compared with the pulse width, the smaller the transient response will be when compared with the constant plateau. Operational radars have no way of knowing when a target is fully illuminated, but because the transient response is significantly shorter than the steady-state, it is usually assumed that measurements are consistently taken during steady-state.

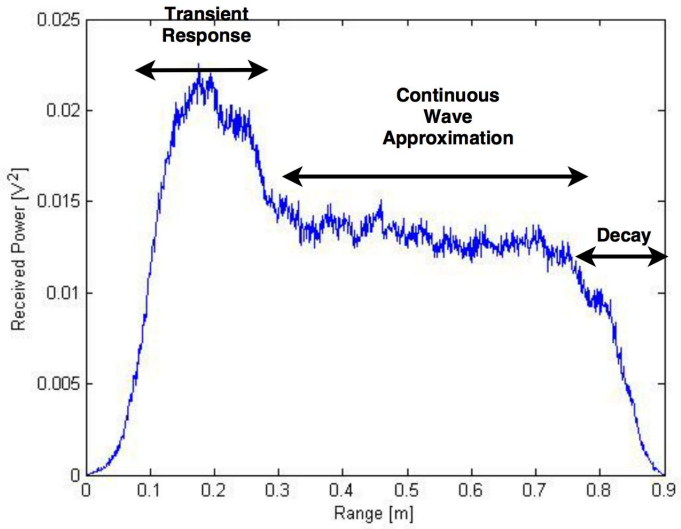

Figure 4.13: Measured radar return of 6-inch sphere (5 ns pulse)

The LVRTS's pulse width may be adjusted between 1 and 5 nanoseconds. However, because of the expected small RCS of UAVs, a 5 nanoseconds pulse is necessary to increase the SNR to acceptable levels. The 5 nanosecond pulse width does not allow sufficient range resolution to identify scattering centers or to build radar images. Neither is the pulse long enough to ensure that the UAV is fully illuminated: induced currents will still be in a transient mode. As such, the Dynamic RCS Measurement System unfortunately falls between both categories of time-domain analysis.

Because radars aimed at detecting mini-UAVs require a good range resolution, a *relaxation* of the continuous-wave (steady-state) requirement of RCS measurements is made, and the transient response is not disregarded. The Dynamic RCS Measurement System performs a cross-correlation of a square pulse and the returned power signal obtained by adding the squares of the in-phase (I) and quadrature (Q) channels of the receiver. The square pulse has a length of:

$$L_{pulse} = 0.75 + L_{target} \tag{4.2}$$

where L_{pulse} is the correlation pulse length in meters and L_{target} is the maximum dimension of the UAV in meters. The value 0.75 is obtained by computing the pulse length of a 5 pulse and dividing by two because of the pulse

delay ranging. The maximum of the correlation is the raw RCS value. The calibrated RCS value is obtained using Equation (2.13). This measurement scheme has the advantage of providing a good measure of how much energy is truly returned towards the radar for typical operational environments.

RCS Measurement Example

An example of detection and RCS measurement is shown. The raw RCS value measured by the Dynamic RCS Measurement System is computed using:

$$\sigma = max[rect * p_r] \tag{4.3}$$

where p_r is the received power, $rect$ is a rectangular pulse of length given by Equation (4.2) and "$*$" is the cross-correlation operand. The received power p_r is given by:

$$p_r = I^2 + Q^2 \tag{4.4}$$

where I and Q are the in-phase and quadrature-phase channels, respectively.

Suppose the radar receives the return shown in Figure 4.14 when measuring the RCS of a target.

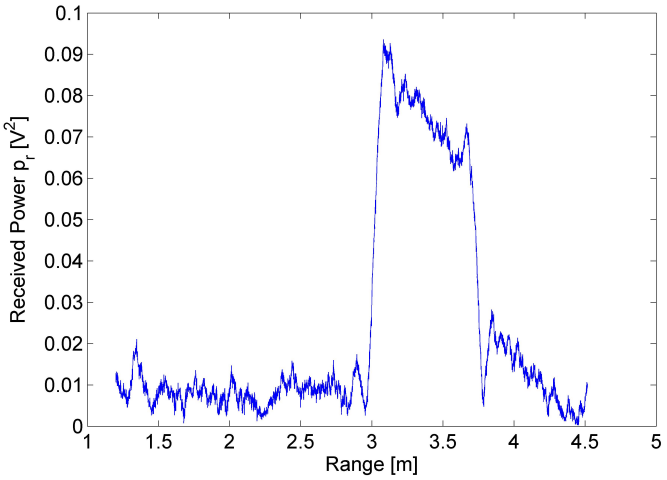

Figure 4.14: Received power versus range

Because the expected maximum target size is 0.15 m, Equation (4.2) is used to determine that the rectangular pulse $rect$, shown in Figure 4.15, has a length of 0.9 m.

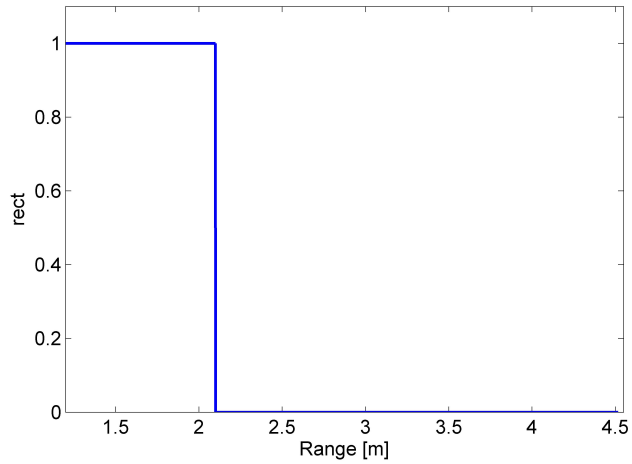

Figure 4.15: Square pulse used for RCS measurement convolution

Figure 4.16 shows the result when performing the cross-correlation of both signals, p_r and *rect*. The measured uncalibrated (raw) RCS is the maximum of the curve, in this case 4.242 m^2 at a range of 2.907 m. Equation (2.13) may then be used to obtain the calibrated RCS.

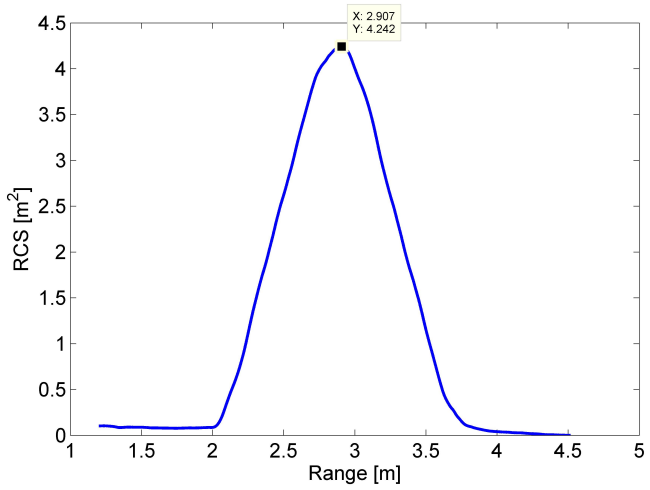

Figure 4.16: Measured RCS versus range

4.8 The Statistical Analyzer

The *Statistical Analyzer* is a custom-written Matlab^{TM} program used by the operator to perform a statistical analysis of the RCS data collected by the *Radar Processor*. The program has a graphical user interface and most statistical parameters are user-selected.

4.8.1 Intra-Bin PDF

The first task of the *Statistical Analyzer* is to determine a PDF to accurately represent the data within a user-defined aspect angle bin. To do so, the script fits an optimal Lognormal, Exponential, Weibull and Gamma PDF to the data by maximizing the likelihood function as described in Section 2.4.1. Then the scripts selects the PDF with the minimal AIC using equation (2.10).

The parameters, mean, variance and percentiles of the selected PDF are then provided to the user. Because the data is left-censored, the sample statistics (mean, variance, percentiles) of the raw data cannot be provided.

To graphically show the goodness-of-fit of the PDF with respect to the raw data, a quantile-quantile (QQ) plot is shown using the Michael-Shucany method [45] with a constant of 3/8, yielding a graphic similar to Figure 2.5. The QQ plot allows the operator to determine how well empirical quantiles correspond to expected quantiles of the fitted PDF. The goodness-of-fit is especially important when making statistical predictions of the UAV's RCS. For example, a probability of detection that relies on the occurrence of high RCS values requires a good estimation of the tail, which is difficult when fitting data to a heavy-tailed PDF like the lognormal because the tail might be under-sampled.

As described in Section 2.5.1, RCS measurements may be left-censored. If the radar range and the optical range disagree by more than some user-defined threshold, the *Statistical Analyzer* considers that clutter has been measured instead of the UAV. In this case, the measured RCS value fed to the PDF fitting algorithm is less than the RCS of the detected clutter. The Matlab scripts used to determine the maximum likelihood parameters of the PDF based on censored measurements can be found at reference [46].

4.8.2 Full UAV PDF

Once a PDF is selected for every user-defined bin, a PDF to represent the whole UAV is sought. Four methods are investigated and presented within this thesis. As mentionned in Section 2.5, no literature was found on this

topic. Results of the four methods will be presented in Section 5.3 when measuring the AR.Drone.

The Single Bin Method

The first method consists of approximating that all measurements were spread uniformly around the target, which is equivalent to considering that all aspect angles of the UAV are grouped in a single bin. A PDF is fitted over all measurements as was the case for the intra bin PDF. The advantage of this method is a simplified statistical analysis. The disadvantage is that the RCS from some aspect angles may have been measured more often, resulting in the skewing of the final result. To determine how well the selected PDF fits the measurement, the Michael-Shucany method of QQ plotting is used [45]. Confidence intervals for the PDF parameters may be computed using the likelihood ratio test (see Section 2.4.1).

A PDF of Bins' Median, Mean or Mode

To remove the skewing of the full-UAV PDF towards the RCS of the bins observed the most, the second method selects the median, mean or mode of the intra-bin PDF as the bin's representative. All the representative values are then grouped together and a PDF is fitted over the dataset. This method has the advantage of simplicity, yet the variance of the final PDF will be reduced due to the averaging within each bin. This will artificially lower the probability of detection for low SNRs.

If the bin's representative is the mean and the intra-bin PDF is lognormal, a 95% confidence interval on the means can be obtained by using El-Shaarawi normal approximation of Equation (2.15).

A PDF for the Average of Lognormal Random Variables

If we can approximate that the PDF within each bin is lognormal, reference [47] shows that the sum of their underlying random variable may be approximated by using a lognormal PDF with good results. This method may be adapted to model the average of lognormal random variables instead of the sum and thus provide a PDF for the full UAV.

Let X_i be the lognormal random variable that represents the RCS in the i^{th} bin. Define the random variable Y that represents the RCS of the overall UAV. The location and scale parameters μ_{full_uav} and σ_{full_uav} of the lognormal PDF of Y are sought. The approach is based on [47] with slight modifications of the nomenclature. For clarity purposes, the RCS is represented by the letter

y in the following derivation and the hat operator ($\hat{}$) is used to specify an estimator.

For k equiprobable bins, the random variable Y is defined as:

$$Y(y) = \sum_{i=1}^{k} \frac{1}{k} X_i(y; \mu_{bin_i}, \sigma_{bin_i}) \tag{4.5}$$

where μ_{bin_i} andσ_{bin_i} are the location and scale of the lognormal random variable X_i modeling the RCS of the ith bin.

The random variables Y may be approximated by a lognormal random variable $\hat{Y}$ by matching the Moment Generating Functions (MGF) of both sides of equation (4.5). We are seeking the values of μ_{full_uav} and σ_{full_uav} that minimize the error ϵ given by:

$$\epsilon(y) = \hat{Y}(y; \mu_{full\_uav}, \sigma_{full\_uav}) - \sum_{i=1}^{k} \frac{1}{k} X_i(y; \mu_{bin_i}, \sigma_{bin_i}) \tag{4.6}$$

The MGF is given by:

$$\psi(s) = \int_0^\infty \exp(-sy) p(y) dy \tag{4.7}$$

Replacing $p(\sigma)$ with the definition of the lognormal PDF, we obtain:

$$\psi(s) = \int_0^\infty \exp(-sy) \frac{1}{\sigma_Y \sqrt{2\pi} y} \exp - \frac{(\ln(y) - \mu_Y)^2}{2\sigma_Y} dy \tag{4.8}$$

where μ_Y and σ_Y are the location and scale of the underlying lognormal PDF. We perform the change of variable given by:

$$z = \frac{\ln(y) - \mu_Y}{\sqrt{2}\sigma_Y} \tag{4.9}$$

and use the Gauss-Hermitte integration to obtain the MGF of the left-hand side of Equation (4.5):

$$\hat{\psi}(s) = \sum_{n=1}^{N} \frac{w_n}{\sqrt{\pi}} \exp(-s \exp(\sqrt{2}\sigma_Y a_n + \mu_Y) \tag{4.10}$$

where a_n and w_n are the Gauss-Hermitte abscissas and weights for the order N.

Because the X_i are statistically independent, the MGF of the right-hand side of equation (4.5) is the product of the MGF of the operands. We obtain:

$$\hat{\psi}(s; \mu_{full\_uav}, \sigma_{full\_uav}) = \prod_{i=1}^{k} \hat{\psi}_i(s; \mu_i, \sigma_{bin_i}) \tag{4.11}$$

where $\hat{\psi}$ is defined in equation (4.10), σ_{bin_i} is the scale of the i^{th} bin lognormal RV and μ_i is given by:

$$\mu_i = \mu_{bin_i} + \ln(1/k) \tag{4.12}$$

where μ_{bin_i} is the location of the i^{th} bin lognormal RV.

In order to solve for μ_{full_uav} and σ_{full_uav} in (4.11), two values of s are chosen and a system of two equations with two unknowns,μ_{full_uav} and σ_{full_uav}, is obtained. The choice of the values of s is discussed in [47], with the authors suggesting values of 0.001 and 0.005 to better approximate the head of the CDF (low RCS values) and 1 and 0.2 for the tail of the CDF (high RCS values).

Generating Points based on Bins' PDF (Monte Carlo)

The fourth method consists of using Matlab to generate an equal number of values for all bins by using the computed intra-bin PDFs. A full-UAV PDF is fitted on the combination of all generated values. Because each bin now has the same number of values, bins that initially had more measurements are not favored. However, this method relies on Matlab's ability to generate random points based on each intra-bins PDF.

4.9 RCS Measurement System Validation

This section aims to validate the system's detection and measurement of the RCS by comparing static measurements with the results obtained in the anechoic chamber. To do so, a modification is made to the Dynamic RCS Measurement System to take static measurements.

4.9.1 Modified Dynamic RCS Measurement System

In order to take static measurements using the Dynamic RCS Measurement System, the UAV is placed on a custom-made target stand that rotates in yaw by increments of one degree. The rotation is controlled via a Motion Testbed, just like the custom antenna turret. Figure 4.17 shows the AR.Drone on the custom-made target pedestal. The Motion Testbed is slightly visible between

the absorber and the UAV. Vectorial background subtraction is used to remove the contribution of the target stand and background.

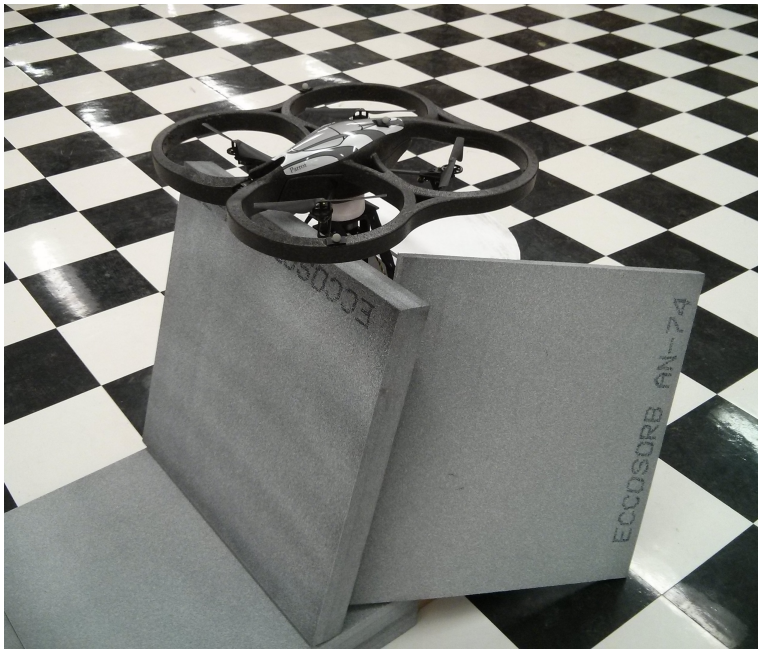

Figure 4.17: AR.Drone on custom-made target pedestal

Table 4.1 shows the parameters of the lognormal PDFs fitted on the static measurements using the Modified Dynamic RCS Measurement System and the anechoic chamber. Due to the assumed symmetry of the AR.Drone, measurements were only taken at yaw angles ϕ between 0 and 180 degrees.

Table 4.1: Static VV measurement campaign results

	LVRTS		Anechoic	
Frequency [GHz]	μ	σ	μ	σ
8	-4.62	0.85	-5.17	1.39
8.5	-4.57	0.94	-4.74	1.33
9	-4.64	0.89	-4.61	1.26

4.9.2 Comparison Between Static Modified Dynamic RCS Measurement System and Anechoic Chamber Results

Figure 4.18 shows the static RCS versus yaw angle of the AR.Drone using both measurement methods at 8.5 GHz using a vertical polarization.

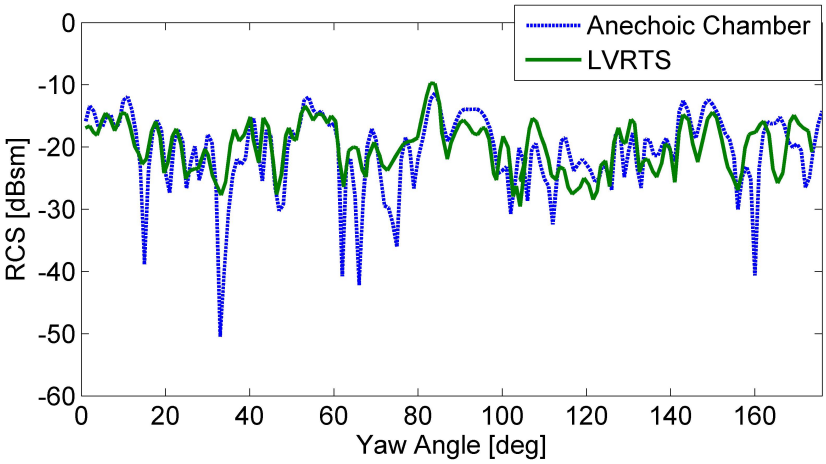

Figure 4.18: Static RCS measurements at 8.5 GHz

The results show good agreement between the curves with a mean difference of 0.8 dB and a linear correlation coefficient of 0.6. This implies that the Dynamic RCS Measurement System is capable of accurately measuring RCS. The sharp nulls measured in the anechoic chamber are not visible when using the modified Dynamic RCS Measurement System due to the presence of more thermal noise and the smaller dynamic range. The impact of the lack of sharp and deep nulls on the LVRTS curve is discussed in Section 5.4. Furthermore, the weight of the AR.Drone makes the Motion Testbed tilt slightly depending on the yaw angle, which in turn modifies the pitch angle. Finally, the measurements in the anechoic chamber were taken in the continuous-wave frequency domain whereas the UAV was illuminated by a pulse when using the Dynamic RCS Measurement System and never reached the steady-state as described in Section 4.7.2.

4.10 Summary

The Dynamic RCS Measurement System was designed to merge real-time positional data of the UAV with its radar return. The Optitrack^{TM} infrared camera tracking system is used to track the UAV and the LabVolt^{TM} Radar Training System to measure the RCS. Matlab^{TM} was chosen to interface both systems and save the results.

The measurements are then statistically characterized using Matlab^{TM} to compute a single full-UAV PDF of the RCS. Four methods may be used to compute the PDF and their differences will be investigated in the next chapter.

To validate the system, static measurements were taken using a modified Dynamic RCS Measurement System and compared with anechoic chamber measurements. The results from both methods show good correlation and the differences may be explained by the greater sensitivity of the anechoic chamber, variations of the pitch angle and the different RCS measurement methodology. Overall, the Dynamic RCS Measurement System seems appropriate to measure the RCS of mini-UAVs.

5 Dynamic RCS Measurements

This chapter presents a measurement campaign aimed at dynamically measuring the RCS of the Parrot^{TM} AR.Drone using the Dynamic RCS Measurement System described in Chapter 4. Sections 5.1 and 5.2 present the configuration and calibration of the measurement system, whereas Section 5.3 presents the results. Finally, static and dynamic results are compared in Section 5.4.

5.1 System Configuration

The Dynamic RCS Measurement System has been designed and built such that the operator has control over many system parameters related to data collection and analysis. Different targets, environments and the desired precision lead to different configurations. This section describes how the system was configured to measure the dynamic RCS of the AR.Drone in particular and explains the rationale behind the decisions.

5.1.1 Radar Settings

To ease the detection of the UAV's radar return, the pulse width is maximized to 5 nanoseconds. The range span is also maximized to 7.2 m so that the UAV is never out-of-range within the room. With this range span, the range resolution is 0.7 cm. The PRF was set to the highest value available from the LVRTS, 288 Hz, because a high PRF has the effect of speeding up measurement campaigns, reducing the coordination error between the optical system and the radar and improving the SNR for a given radar integration time. Table 5.1 summarizes the configuration of the radar.

Table 5.1: Radar configuration

Pulse Width	5 ns
PRF	288 Hz
Frequency	8-10 GHz
Range Span	7.2 m

5.1.2 Tektronix DPO4104 Oscilloscope

The DPO4104 oscilloscope is set to a sampling rate of 2.5 megasamples per second and a record length of ten thousand samples, allowing the visualization of the full range span on a single trigger event. At this sampling rate, the range bin length is 0.83 mm. The radar I and Q channels are sampled in channels 1 and 2 respectively. Channel 3 samples the radar PRF clock and triggers on a rising edge. Channels 1 and 2 are AC coupled to remove any DC bias from the radar whereas channel 3 is DC coupled.

5.1.3 *Radar Processor*

UAV Range and Altitude

The minimum range is driven by the custom antenna turret beamwidth and far-field requirements.

With a beamwidth of 12 degrees in yaw and a maximum cross-range dimension of 0.68 m (the diagonal of the AR.Drone), the minimum range should be 3.25 m for the UAV to be fully within the -1 dB bandwidth of the custom antenna turret. However, the extremities of the AR.Drone are mostly composed of air, styrofoam and parts of the plastic propeller. A finite-element simulation (see Section 2.2) was performed to determine the RCS of the 20-cm long propeller using the model of Figure 5.1. The ABC used for the simulation is a PML. Figure 5.2 shows the propeller's RCS against the yaw angle at 8 GHz using a VV polarization. The RCS is, at most, -39 dBsm. Even if the contribution of the four propellers were added in phase at that maximum value, the RCS would be no higher than -33 dBsm. This simulation implies that the maximum dimension of the UAV can be approximated by removing the propellers. The maximum dimension of the AR.Drone then becomes 36 cm (the distance between diagonally-positioned propeller engine). Because of these results, the minimum range could be reduced to 1.7 m.

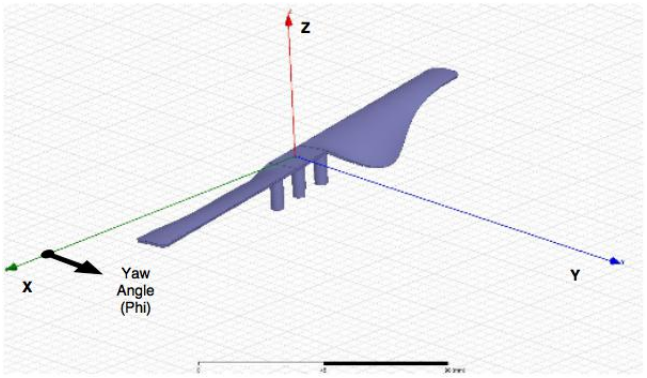

Figure 5.1: Computer model of the AR.Drone propeller

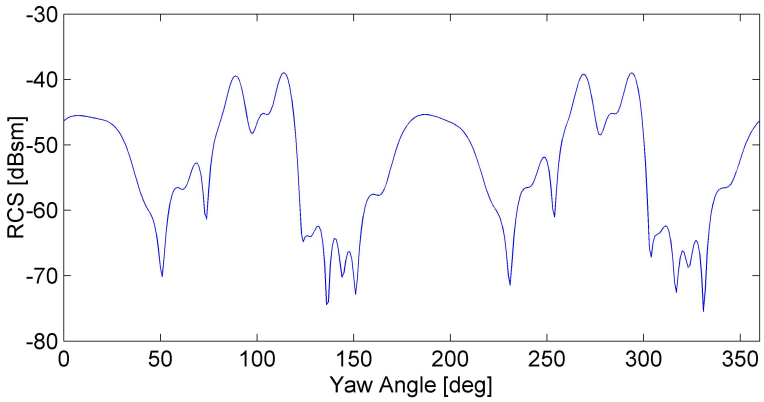

Figure 5.2: Simulated static RCS of the AR.Drone propeller at 8 GHz

Far field requirements state that the UAV must be in the far-field of the transmitter and that the receiver must be in the far field of the UAV. The far field distance d_f in meters is given by:

$$d_f = \frac{2D^2}{\lambda} \tag{5.1}$$

where D is the maximum cross-range dimension of the antenna or target [11].

With a width of 0.076 m, the far-field distance of the transmitting antenna is 0.35 m at 9 GHz. However, with a UAV width of 0.36 m, the far field distance from the UAV is 7.77 m. Nonetheless, the ISAR images from Section 3.3.3 may be used to reduce the far-field distance. Radar images from the front

and broadside of the AR.Drone (see Figures 3.13 and 3.14) show that the most reflective parts of the UAV are within 20 cm in cross-range. As such, the minimum far-field distance becomes 2.4 m. Based on these results, a minimum range of 2.5 m is selected.

The maximum range is determined by visual inspection of the room clutter. By moving the turret manually, it was determined that significant side-wall clutter appears at a range of 5 m, making it the maximum allowable range of the UAV.

To minimize the clutter return from the floor and ceiling, radar returns are not processed if the UAV altitude is not between 0.5 and 2.5 m.

UAV Dynamics

To determine the maximum allowable UAV velocity given the chosen radar integration time of 55.6 ms, the approximate AR.Drone ACF is computed. The longest dimension of the drone is 0.68 m. By using equation (2.12) at 9 GHz, a decorrelation angle of 0.0245 radians (1.4 degrees) is obtained. For a drone flying at a constant speed perpendicular to the line of sight of the radar, the maximum change of aspect angle will occur when the target is closest to the radar. Using a minimum distance of 2.5 m, a cross-range distance of 0.06 m is computed. This amounts to a maximum allowable UAV speed of 1.08 m/s. Figure 5.3 highlights the geometry behind this result. In order to account for concurrent variations in yaw, the maximum speed is limited to 0.3 m/s.

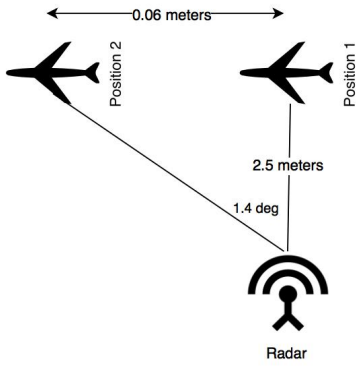

Figure 5.3: Decorrelation calculation

Detection

Detection is performed as explained in Section 4.7. The length of the correlation pulse is 1.43 m, as given by Equation (4.2) with the maximum dimension of 0.68 m of the AR.Drone. If the radar and optics range differ by more than 0.4 m, the RCS is saved as a censored measurement. This value represents a compromise between accounting for timing errors between the optical and radar systems and obtaining the highest possible amount of uncensored data for post processing.

5.1.4 *Turret Controller*

The *Turret Controller* is set to track the UAV automatically using the Optitrack^{TM} data, without input from the operator.

5.2 Calibration

In addition to configuring the system appropriately, various sub-systems of the Dynamic RCS Measurement System must be calibrated to ensure consistent results. This section provides the necessary details and procedures related to calibration.

5.2.1 I/Q Balancing

The LVRTS is a coherent radar and, as such, requires precise calibration of its I and Q channel gain to ensure that they match precisely. Mismatched I and Q gains would result in the measured RCS becoming a function of the range. A way of calibrating the channel gain is to move a target and adjust the gain in each channel so that the measured RCS is constant notwithstanding the range to target. However, moving the target would imply that other sources of errors, such as tracking errors, may become an issue. To remove those errors, I/Q balancing is performed by electronically delaying the radar return signal using the Colby Instruments CPDL100a Programmable Delay Line [48]. The schematics of the modified system is shown in Figure 5.4.

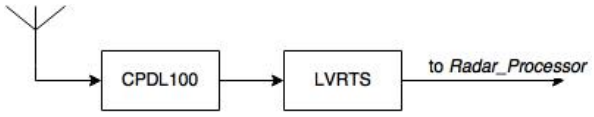

Figure 5.4: Schematic of modified system for I/Q calibration

Delays between 0 and 160 ps are used and the I/Q ratio is adjusted to obtain the smallest variance in the measured RCS. Figure 5.5 shows the RCS of a six-inch sphere as a function of the delay after I/Q balancing. The result has a maximum variation of less than 1 dB.

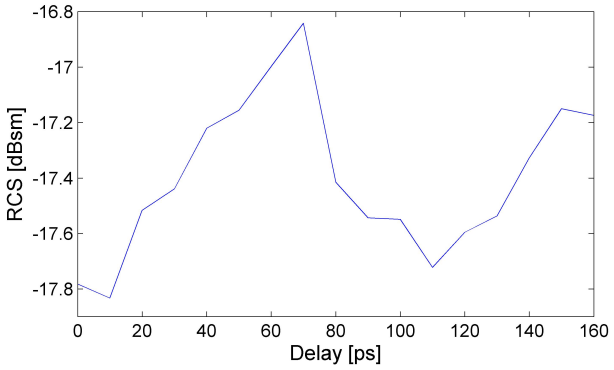

Figure 5.5: RCS versus delay of a 6-inch sphere at 8 GHz

The variations in the measured RCS may be explained by the gain variation of the CPLD100 versus the delay. Measurement of the transmission coefficient s_{21} of the CPLD100 versus the delay reveals that the gain varies by 1 dB depending on the delay. The remaining variations of the sphere's RCS may be attributed to thermal noise and a slight variation in the room return depending on the delay.

Section 5.2.6 will further examine the impact of I/Q balancing on the measured RCS of a six-inch diameter sphere.

5.2.2 Custom Antenna Turret Boresight Calibration

Boresight calibration is necessary to ensure that the UAV is tracked at the maximum of the antenna pattern. As discussed in Section 4.4, the boresight calibration is not overly sensitive due to the -1 dB beamwidth being seven degrees in elevation and twelve degrees in azimuth. However, when detecting objects of small RCS like the AR.Drone in a cluttered environment, maximizing the turret gain increases the SNR.

The boresight calibration is performed by manually scanning the turret in elevation and azimuth and measuring the power return of a six-inch sphere. The turret is aligned with the sphere by seeking the turret position of maximum return. Once the custom antenna turret is aligned with the sphere, the sphere is removed and replaced by the UAV and the *Turret Controller* begins

tracking the drone as discussed in Section 4.6. Figure 5.6 shows the *Turret Controller* during boresight calibration.

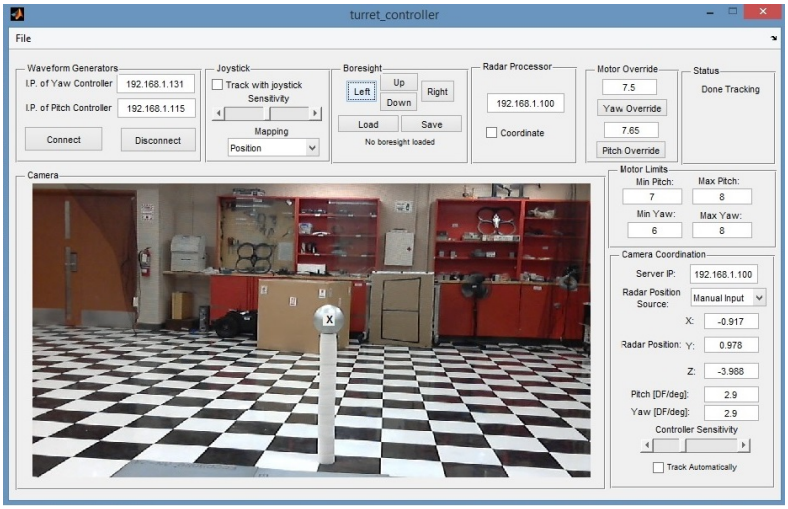

Figure 5.6: Turret boresight calibration

5.2.3 Power Calibration

To calibrate the power levels measured by the radar, an object of known RCS (for example a six-inch metallic sphere) is measured first, and the UAV's RCS is calculated based on this known value using Equation (2.13). Background subtraction is used to remove the return of the pedestal and the room.

To determine the accuracy of the power calibration, the RCS of a 3-inch diameter metallic sphere is measured. The analytical RCS of the 3-inch sphere is 0.0042 square meters (-23.8 dBsm) at 8 GHz. An RCS of 0.0044 square meters (-24.5 dBsm) is measured using the Dynamic RCS Measurement System. This result confirms that the power calibration is acceptable given the error of 2 square cm (-37 dBsm). This 5% error is acceptable given the RCS of the AR.Drone measured in the anechoic chamber. As shown in Figure 3.7, the expected RCS of the AR.Drone is roughly between -12 and -25 dBsm, with only 8 measurements falling below -25 dBsm. The -37 dBsm error is 16 times smaller than that threshold.

5.2.4 Radar Range Trace Calibration Using Optitrack Data

The LVRTS does not provide the absolute range associated with each radar return sample. In order to build a radar range axis, it is necessary to use the Optitrack^{TM} System. The same process is used as for the power calibration. Infrared markers are placed on the six-inch sphere and background subtraction allow to accurately determine the location of the sphere on the radar trace. This location is then correlated with the range measured using the Optitrack^{TM} data. Because the oscilloscope provides the time of each samples, other bins' range may be computed. Building an accurate radar range axis is necessary to determine if the measured RCS of the in-flight UAV is censored.

5.2.5 Room Background Subtraction

As mentioned in Section 4.7, background subtraction is performed by saving range traces of the empty room against the duty factors (DF) of the azimuth and elevation controller of the custom turret and then performing a vector subtraction during the measurement campaign. Each set of DF represents a turret pointing angle. However, the Motion Testbed has shown during experimentation a slight slippage of the servos, which means that sending the same duty factors to the turret at different times may result in a slightly different turret orientation. This impedes the use of background subtraction during in-flight measurements and forces the operator to only fly the UAV in areas of low clutter within the room.

To fix this issue, a replacement of the Motion Testbed by a more precise radar-grade turret would be necessary. For the AR.Drone measurement campaign, background subtraction was not used for in-flight measurements.

5.2.6 Calibration Validation

In order to ensure that the system is configured and calibrated correctly, a variance test is performed. The six-inch sphere and its pedestal are manually moved throughout the room and automatically tracked by the *Turret Controller*. The RCS is measured for every position. This test determines whether the automatic tracking is working correctly and verifies that the I and Q channels are balanced. Figure 5.7 shows the measured RCS at 8 GHz wih a VV polarization versus the range. Note that each measurement was taken at a different turret pointing angle.

The maximum error is 29 cm^2 (-25.7 dBsm), but the mean error is only 11.3 cm^2 (-29.6 dBsm). Just as was the case for the power calibration, this

error is deemed acceptable to proceed with the measurement campaign of the AR.Drone due to the lower threshold of −25 dBsm that is expected. Furthermore, because statistical processing requires a high number of measurements, the impact of the error is minimized.

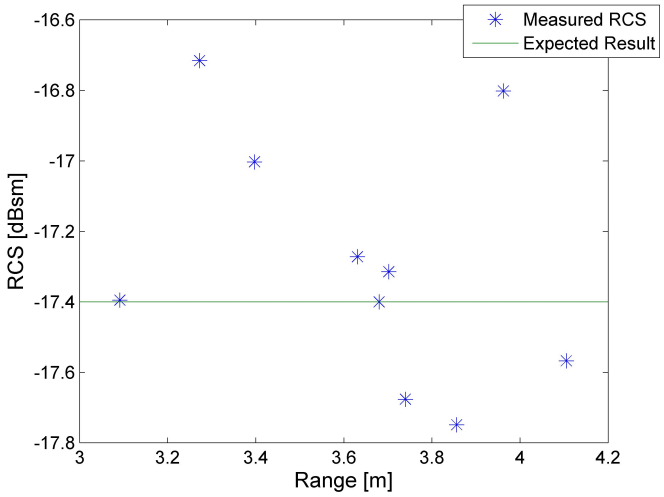

Figure 5.7: Measured RCS of six-inch sphere versus range for random pointing angles at 8 GHz

5.3 Results

The measurement campaign was performed at the Royal Military College of Canada (RMCC) in the Fall of 2015. Measurements were taken at 8, 8.5, 9 and 9.5 GHz using VV polarization and at 8.5 GHz only using HH polarization. The measurement for each frequency and polarization took on average half a day, including the calibration time. Because the AR.Drone is assumed symmetrical, data was only collected for yaw angles ϕ between 0 and 180 degrees. This section highlights the results from the campaign.

5.3.1 Investigation of Full-UAV PDF Computation Techniques

The various ways of computing the full-UAV PDF described in Section 4.8.2 are investigated by using the data set at 8 GHz with a VV polarization as

an example. The data set contains 1455 measurements, of which 393 are censored. The smallest uncensored measurement is −26 dBsm. However, the amount of clutter varies widely depending on the turret position, as evidenced by a censored −10 dBsm measurement.

Figure 5.8 shows the number of measurements per yaw angle. There are more measurements between 80 and 90 degrees than at other angles, leading to an expected bias of the PDF towards the RCS around broadside.

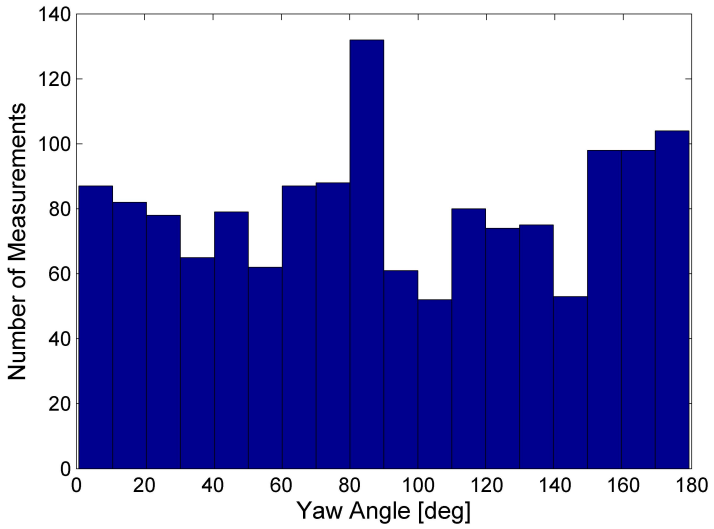

Figure 5.8: Measurement distribution for 8 GHz VV campaign

The Single Bin Method

By using the single bin method, the PDF with the smallest AIC is a lognormal with a μ of −3.94 and σ of 0.69. The lognormal AIC is −5216 and the second best fit, a Weibull distribution, has an AIC of −5084. The fitted lognormal distribution represents the dynamically obtained RCS of the AR.Drone for the specific flight pattern that was flown during measurements.

Figure 5.9 shows the QQ plot between the expected quantiles of the fitted lognormal distribution and the measured quantiles. The PDF represents the measurements well until the 99th percentile, with an error of 53 cm^2 at that percentile.

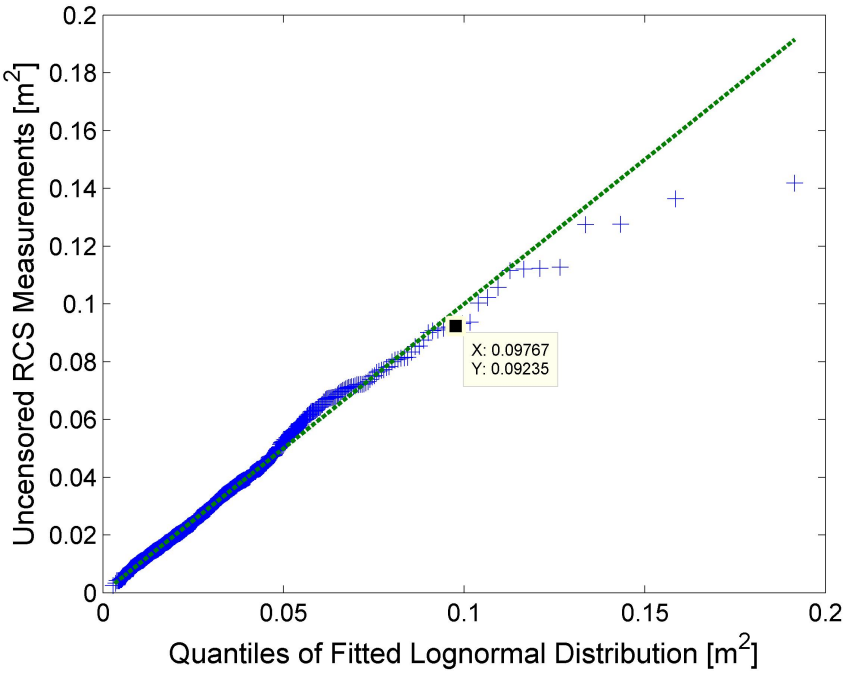

Figure 5.9: QQ plot of 8 GHz VV measurements

A PDF of Bins' Mean

Using yaw angle bins of ten degrees and no binning in pitch, the RCS mean of the lognormal PDF fitted within every bin is plotted against the yaw angle ϕ in Figure 5.10. The percentiles are those of the fitted PDF within each bin and the 95% confidence interval is based on Equation (2.15). The RCS is maximized at broadside ($\phi = 90\,\text{deg}$) with a mean of -13 dBsm and at the front ($\phi = 0\,\text{deg}$) and tail ($\phi = 180\,\text{deg}$) of the UAV with means of -15 and -14 dBsm, respectively.

In Figure 5.10, it was assumed that the intra-bin PDF is lognormal. However, only in 9 of the 18 yaw bins does the lognormal PDF minimizes the AIC. Table 5.2 shows the PDF that minimizes the AIC within each bin and its AIC score.

Despite the fact that the lognormal PDF is only chosen for 50% of bins, its AIC score in the bins where it is not selected is typically close to the score of the selected PDF, making the approximation acceptable.

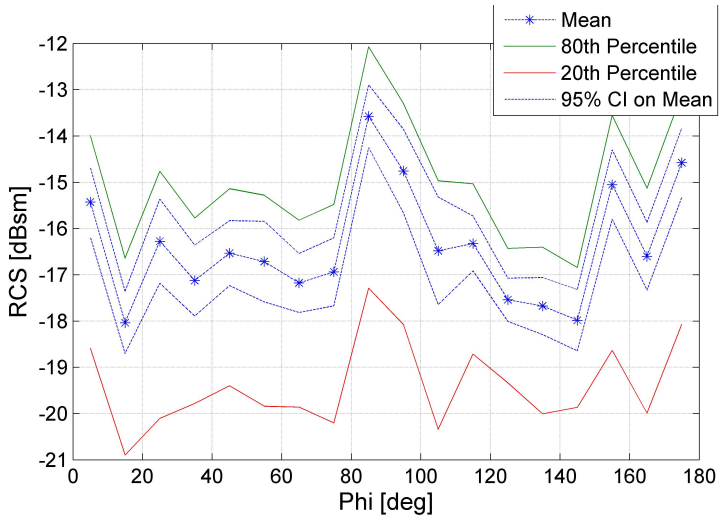

Figure 5.10: Fitted RCS versus yaw angle of 8 GHz VV measurements

Table 5.2: Intra-bin selected PDFs

Bin	Selected PDF	AIC	AIC Difference With Lognormal
0-10	Weibull	−336	7
10-20	Gamma	−226	3
20-30	Lognormal	−263	-
30-40	Lognormal	−196	-
40-50	Lognormal	−127	-
50-60	Gamma	−201	1
60-70	Gamma	−359	1
70-80	Lognormal	−369	-
80-90	Gamma	−418	3
90-100	Lognormal	−217	-
100-110	Weibull	−136	3
110-120	Gamma	−364	4
120-130	Lognormal	−417	-
130-140	Lognormal	−332	-
140-150	Lognormal	−199	-
150-160	Lognormal	−317	-
160-170	Gamma	−292	2
170-180	Gamma	−348	1

The mean from each bin of Figure 5.10 is used to generate a full-UAV PDF. The fitted PDF is again best approximated by a lognormal with a μ of -3.76 and σ of 0.31. Based on these values, it is clear that the variance of the PDF is smaller than the variance of the PDF computed with the single-bin method. Furthermore, because a PDF is fitted to a small sample size (18 samples), the standard error on the estimated parameters is increased. Figure 5.11 visually shows the distribution of means in blue and the fitted PDF in red, highlighting the effect of the small sample size.

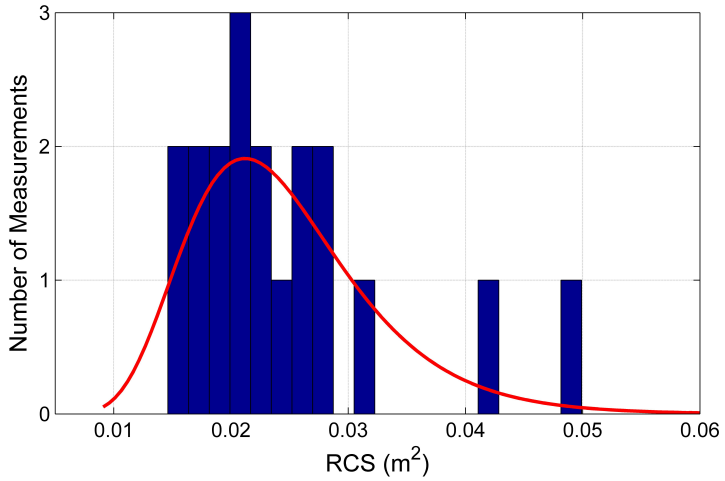

Figure 5.11: Distribution of bins' mean for 8 GHz VV measurements

A PDF for the Average of Lognormal Random Variables

The full-UAV RCS is computed using the average of lognormal random variables of Section 4.8.2. With a Hermitte Integration Order of 10 and using the abscissa values of 0.001 and 0.005 to better approximate the head of the RCS PDF, a lognormal PDF with a μ of -4 and a σ of 0.71 is obtained. These fitted parameters are close to the parameters obtained using the single bin method.

Generating Points based on Bins' PDF (Monte Carlo)

The Monte Carlo analysis described in Section 4.8.2 is performed by generating 50000 points per bin based on a lognormal PDF fitted within every ten degree yaw bin. The result is approximated as a lognormal PDF with μ of -3.94 and

a σ of 0.66. The results are close to the single bin and average of lognormal random variable methods.

Comparison of Full-UAV Methods

Table 5.3 shows the full-UAV parameters for the four different techniques and Figure 5.12 shows the PDFs graphically.

Table 5.3: 8 GHz VV lognormal PDF parameters

Method	μ	σ
1. Single-bin	-3.94	0.69
2. Bin's Mean	-3.76	0.31
3. Average of Lognormal PDFs	-4	0.71
4. Monte Carlo	-3.94	0.66

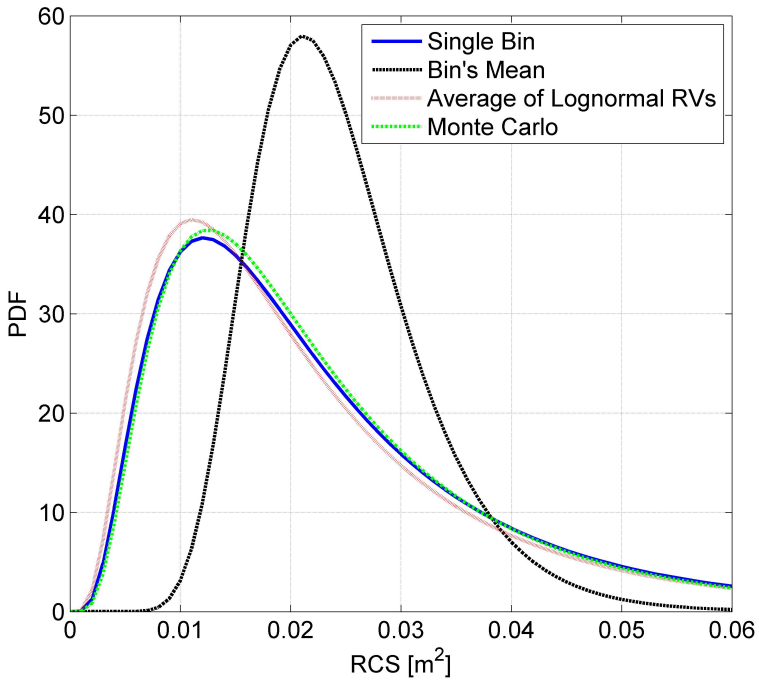

Figure 5.12: RCS PDFs for 8 GHz VV measurements

With the exception of the PDF of bins' mean, the remaining three methods yield a very similar PDF. This result highlights the fact that the PDF of bins' mean method should not be used to generate a full-UAV PDF, as it reduces the variance significantly compared to the other methods. Furthermore, the single-bin method should not be used as it does not account for the flight trajectory during the measurement flight in the generation of a full-UAV PDF. During this measurement campaign, the induced error on the full-UAV PDF of the AR.Drone is reduced because the measurement distribution between each bin of Figure 5.8 is fairly flat, which may not be the case for another measurement flight. Furthermore, the AR.Drone is uniformly shaped, with RCS variations due to aspect angle much lower than expected for different UAVs, which reduces the impact of the flight pattern on the measured RCS. As such, the average of lognormal PDFs and Monte Carlo are recommended when computing a full-UAV PDF. However, the Monte Carlo method will be used for the following analysis because it does not necessarily make the assumption that the PDF within every bin is lognormal.

Notes on the Required Number of Measurements Per Bin

The results from the previous section assume that a sufficient number of measurements were taken within each bin to fit a representative PDF. The minimum number of measurements within a bin in Figure 5.8 is 51 between 140 and 150 degrees in yaw.

Figure 5.13 shows the QQ plot of the fitted PDF within that bin. The measurement quantiles are very close to the expected quantile, meaning that the PDF represents the measurements well.

The QQ plot of Figure 5.13 allows one to determine if the selected PDF fits the measurements well but does not reflect how sensitive the maximum likelihood estimation of the PDF parameters is. The likelihood ratio test described in Section 2.4.1 may be used to construct an approximate 95% confidence interval on the parameters. Figure 5.14 shows a contour plot of the test result for the data within the bin. The innermost circle represents the boundaries of the 95% confidence interval because the 95th percentile of the chi-square distribution with two degrees of freedom is 5.991. From Figure 5.14, μ can vary between -4.4 and -4.08 and σ between 0.32 and 0.57. To tighten the area, more samples would be required.

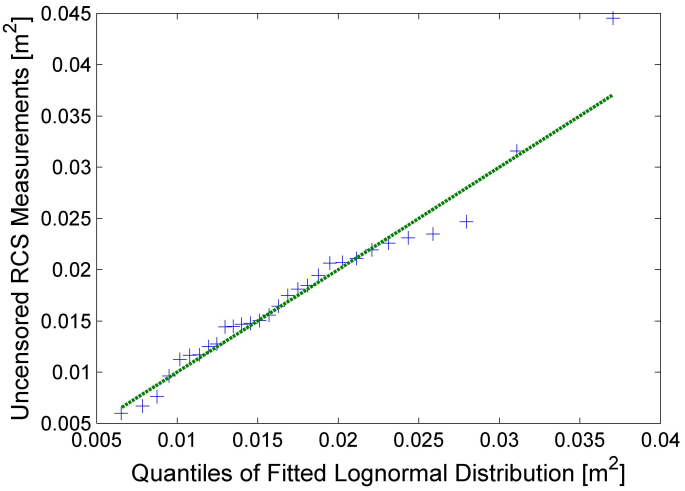

Figure 5.13: QQ plot of measurements between 140-150 degree in yaw

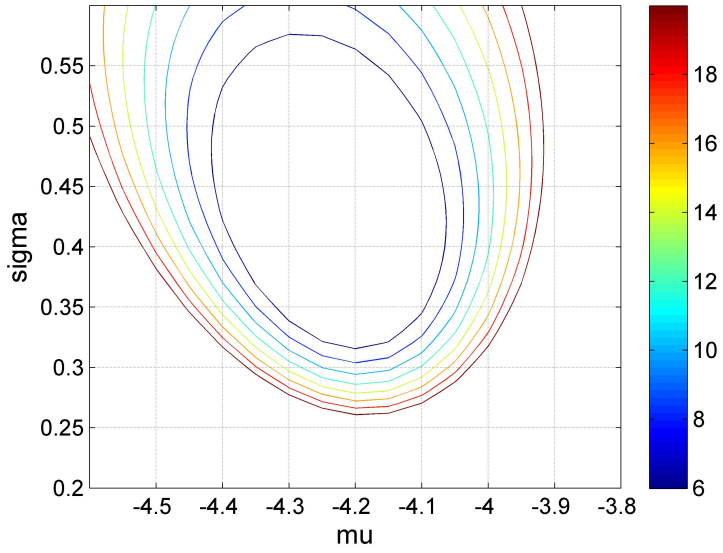

Figure 5.14: Likelihood ratio test for the 140-150 degree yaw bin

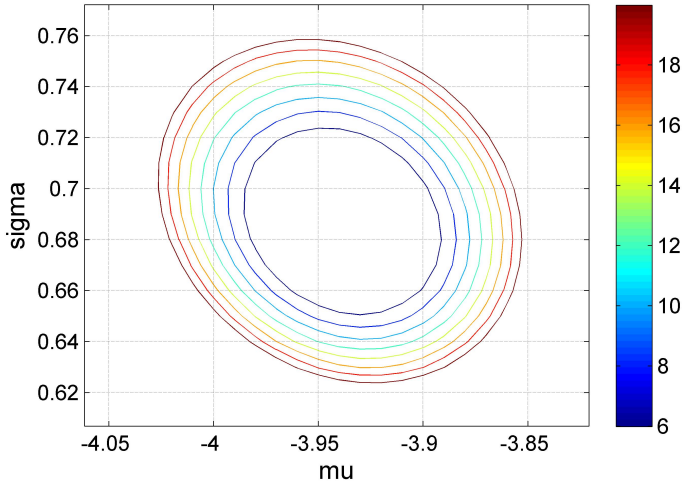

Figure 5.15: Likelihood ratio test for the single bin method

The confidence interval of the single-bin method is shown in Figure 5.15 with the innermost circle representing the boundaries of the 95% confidence interval. From Figure 5.15, μ can vary between -3.98 and -3.89 and σ between 0.65 and 0.72. The confidence interval is much narrower due to the increase in the number of measurements. Nevertheless, the single-bin method should not be used because the fitted PDF models very accurately the RCS of the UAV during the measurement flight, but poorly infers the RCS of the drone during another flight due to the lack of aspect angle information.

5.3.2 RCS at Different Frequencies

The full-UAV PDF computed using the Monte Carlo Method for different frequencies are shown in Figure 5.16 and their parameters are listed in Table 5.4. The yaw bin width is 10 degrees and the number of Monte-Carlo generated points per bin is 10000. Measurements were taken using a VV polarization. The original 8.5 GHz data set contains 2588 measurements, of which 795 are censored and the 9 GHz data set contains 1998 measurements, with 997 censored. Both data sets contain a minimum of 100 measurements per bin.

The 8.5 GHz PDF is the highest for RCS values below 0.01 m^2. Between RCS values of 0.01 and 0.041 m^2, the 8 GHz PDF is highest, followed by the 9 GHz PDF above 0.041 m^2. Based on the results, choosing the radar frequency is not a trivial task.

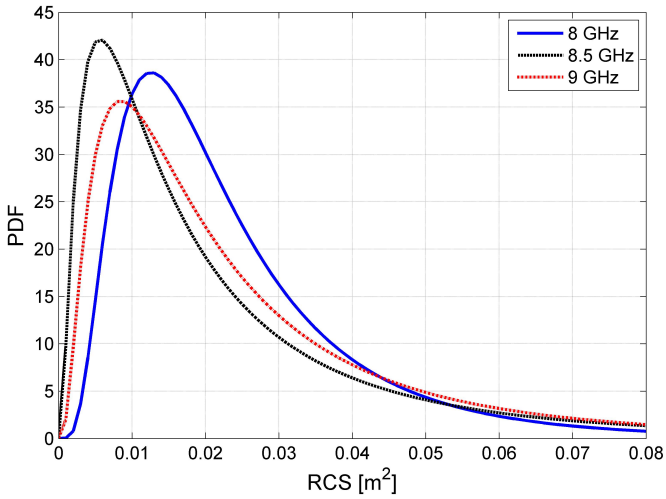

Figure 5.16: Monte-Carlo generated PDFs of VV measurements

Table 5.4: VV PDF parameters

Frequency (GHz)	μ	σ
8	-3.94	0.66
8.5	-4.16	1.01
9	-3.98	0.89

Probability of Detection for Different Frequencies

To determine the optimal radar frequency, the single-pulse probability of detection given the RCS PDFs of Table 5.4 is computed using the method described in Section 2.6. Of note, the resulting probabilities of detection are based on different calibrations to account for radar parameters like the gain that vary with frequency. The probability of detection curves of Figure 5.17 are obtained for a probability of false alarm of 10^{-8}.

For ranges below 11.25 m, the highest probability of detection is obtained at 8 GHz. However, the probability of detection is highest at 8.5 GHz beyond 11.25 m. The selection of the optimal frequency may be based on the needs of the operator. An optimization strategy may be the highest range for a 90% probability of detection for a single pulse. Based on this criteria, the selected frequency would be 8 GHz.

Similarly, binary integration may be factored. Figure 5.18 shows the probability of detection of a 3 of 8 receiver [13]. Based on the curves, the radar should again be tuned at 8 GHz. The advantage of the binary integrator in this scenario is the increase of the 90% detection range from 8.25 to 10.25 m.

Finally, an operator might be interested in the probability that a target will be detected after N pulses. The cumulative probability of detection PoD_c is given by:

$$PoD_c = 1 - (1 - PoD)^N \tag{5.2}$$

where PoD is te single-pulse probability of detection [12]. Figure 5.19 shows the curves for a cumulative probability of detection of ten pulses. In this case, the optimum frequency for a 90% probability of detection is 8.5 GHz, with a detection range of 13 m. Although the full-UAV RCS PDF for the 8.5 GHz measurements is more skewed towards the left than the PDF at 8 GHz, it has a greater variance. This implies that at low SNRs (high ranges), the high variance will increase the probability of detection because it is more likely that a high RCS will be presented to the radar. This is evident from Figure 5.19 which shows the cumulative probability of detection for ten pulses. Even if the 8.5 GHz detection range was on average lower for a single pulse than at 8 GHz, it is now the highest for most probabilities of detection.

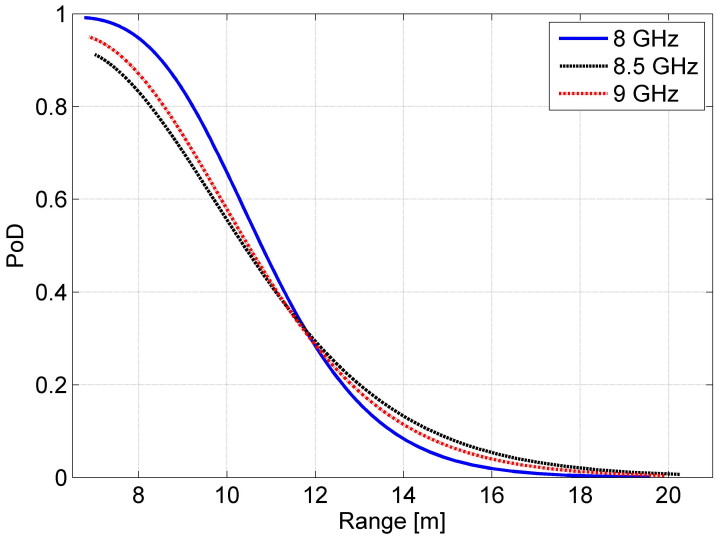

Figure 5.17: Single pulse VV probability of detection

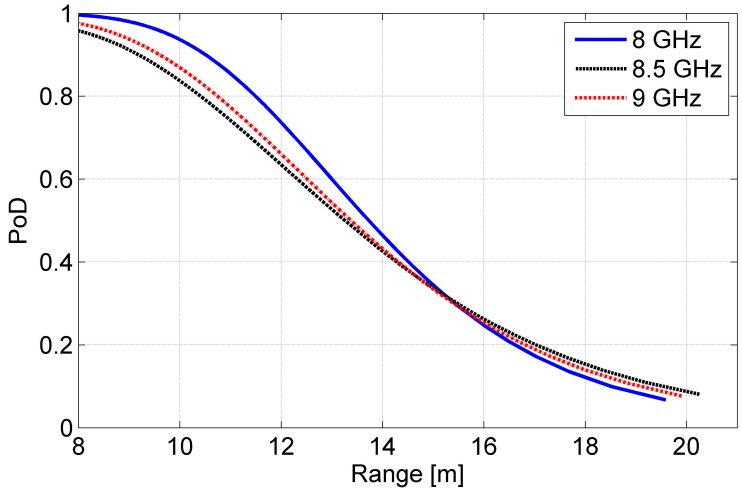

Figure 5.18: Probability of detection for a 3 of 8 detector

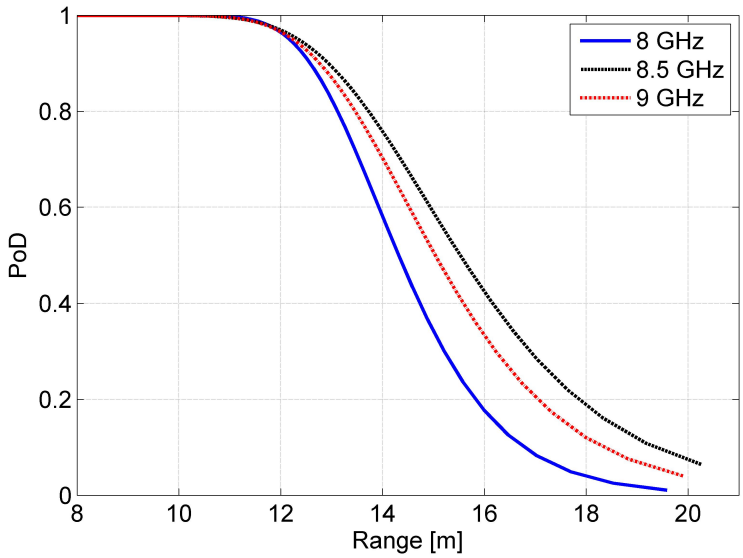

Figure 5.19: Cumulative probability of detection for 10 pulses

These results show that precise knowledge of the RCS distribution is crucial for computing the probabilities of detection for various radar configura-

tions, and that results may sometimes appear counter-intuitive. For example, tuning the radar at 8.5 GHz instead of 8 GHz leads to a 2 m decrease in the single-pulse 90% probability of detection range, which corresponds to a 20% reduction.

5.3.3 RCS at Different Polarizations

In addition to choosing a frequency, it is usually possible to vary the polarization of the radar to improve target detection. By rotating the antennas on the custom turret, measurements were taken at 8.5 GHz using HH polarization. The resulting PDF parameters are displayed in Table 5.5.

Table 5.5: Monte-Carlo generated 8.5 GHz PDF parameters

Pol	μ	σ	Mean [dBsm]	Var [dBsm^2]
HH	-4.55	0.90	-18.0	-35.03
VV	-4.16	1.01	-15.9	-29.29

The full-UAV single-pulse probability of detection based on the Monte Carlo method is shown in Figure 5.20. It shows the UAV is easier to detect using a VV polarization.

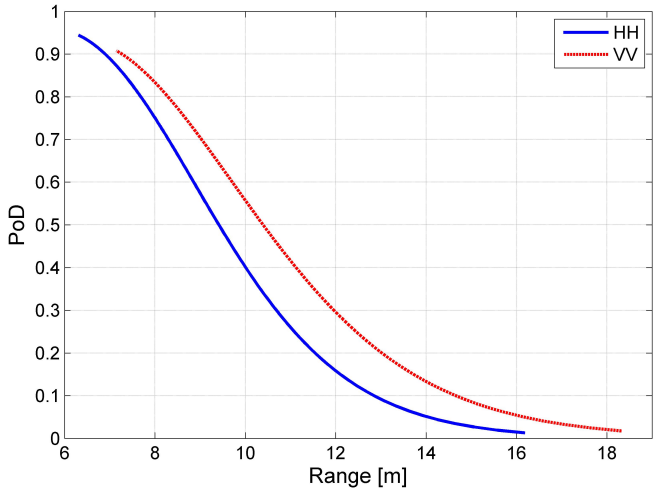

Figure 5.20: Single-Pulse Probability of detection curves at 8.5 GHz

The higher VV RCS seems counter-intuitive due to the longer horizontal dimensions of the AR.Drone. To confirm the results, a ISAR image of the front of the UAV is generated with measurements inside the RMCC anechoic chamber and is shown in Figure 5.21. When compared with the VV results of Figure 3.13, it is evident that the peak RCS is lower by examining and comparing the color scales. Furthermore, the front of the UAV is the area of highest RCS and the core reflects very little.

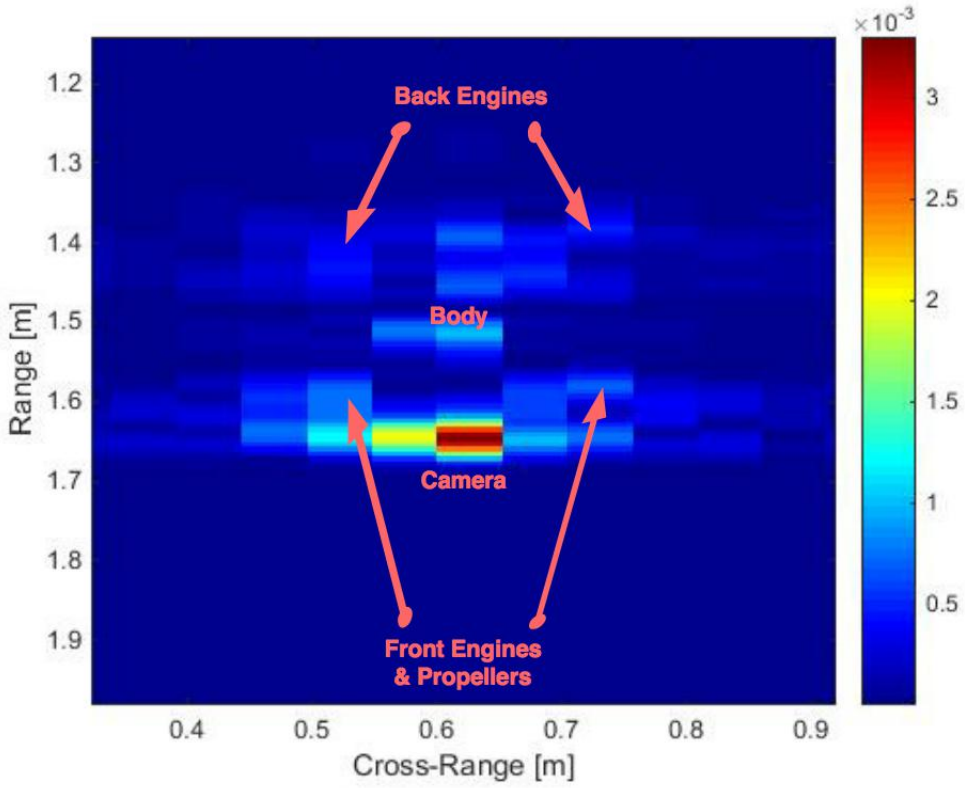

Figure 5.21: HH ISAR image of the front of the AR.Drone

The process is repeated for the side of the AR.Drone and shown in Figure 5.22. The overall shape of the return is similar to Figure 3.14 but the strength is diminished and the cross-range dimension is longer.

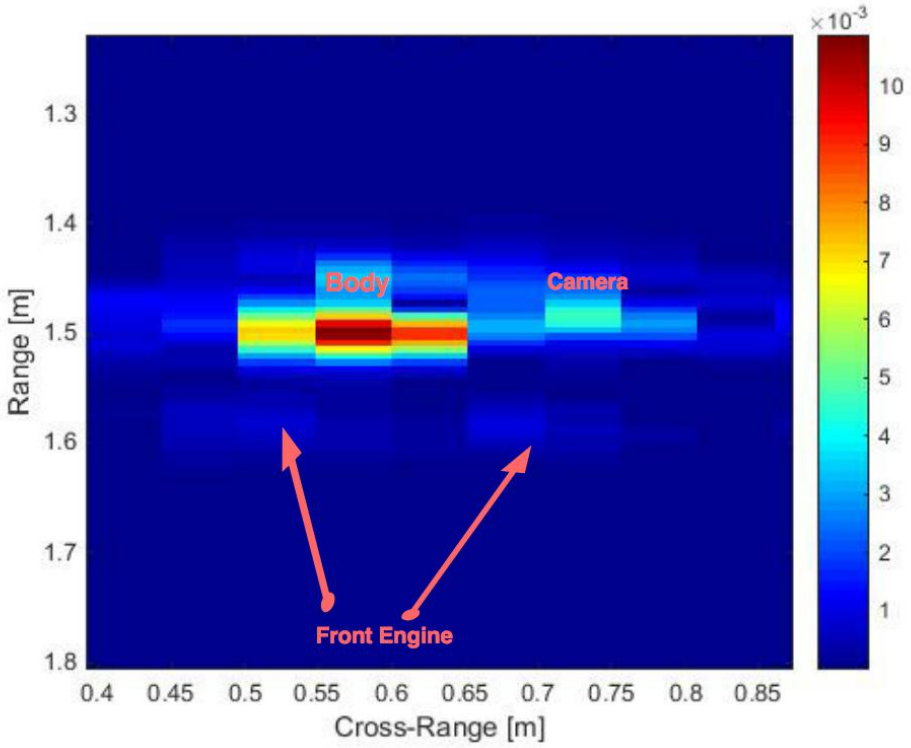

Figure 5.22: HH ISAR image of the side of the AR.Drone

Impact of Clutter on Polarization Selection

It is expected that a higher amount of radar clutter in the room will result in an increase in the proportion of censored measurements during a campaign. Therefore, a count of the number of censored measurements is used to determine the relative amount of clutter when using HH and VV polarizations. HH measurements have 13.8% of censored data, versus 30.71% for VV. Therefore, the amount of room clutter is considered higher when using VV polarization, making HH polarization potentially a better choice to optimize target detection in that specific room. Depending on the operational environment, the amount of clutter may play a significant impact on the polarization selection.

5.3.4 Notes on the Repeatability of Results

To determine the repeatability of the results, two dynamic RCS measurement campaigns are performed at 9.5 GHz for a VV polarization. Table 5.6 lists the results of both measurement campaigns. The second campaign contains more measurements, and the mean of the lognormal full-UAV PDF computed using the Monte Carlo method is slightly smaller.

Table 5.6: 9.5 GHz VV measurement campaigns results

Campaign	Number of Measurements	μ	σ
1	1709	−3.74	0.79
2	1877	−3.98	0.88

Figure 5.23 shows the QQ plot of both experimental data sets. Because the QQ plot is for two experimental data sets, linear interpolation is used for the quantiles of the second data set so that they can be plotted against the quantiles of the first data set. The plot shows good correlation between the expected and the experimental results, with the quantiles of the second data set on average slightly lower than the first.

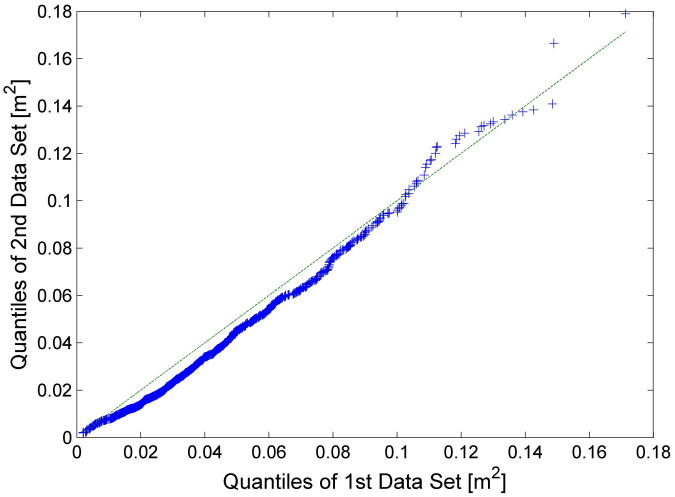

Figure 5.23: QQ plot of experimental data sets at 9.5 GHz VV

Figure 5.24 shows the probability of detection based on the fitted PDFs. As expected from the QQ plot, the second campaign resulted in slightly lower

detection probabilities for the different ranges investigated. The detection range has a maximum difference of one meter for any given single-pulse probability of detection shown on the graph.

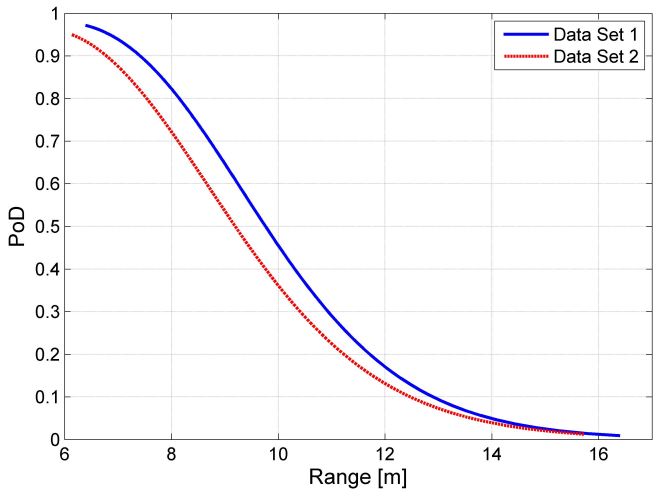

Figure 5.24: Probability of detection of 9.5 GHz VV data sets

The fact that results are not perfectly repeatable when dynamically measuring a target's RCS is often seen as a crippling shortcoming [6]. The use of a full-UAV PDF mitigates the effect of the UAV trajectory on the computed RCS PDF. However, other factors may explain the deficiencies in repeatability:

- The radar transmitter and receiver gains may not be perfectly constant during the measurement campaign;
- Different UAV velocities will lead to different radar integration losses;
- Engines and propellers movement modulates the return echo;
- Different UAV trajectories lead to different turret positions, affecting the amount of clutter;
- Different UAV trajectories and aspects will lead to varying polarization mismatches between the UAV and antenna polarization planes; and
- The exact placement of the battery within the UAV battery compartment changes.

The advantage of the Dynamic RCS Measurement System is that it includes all of these effects for a given flight. Should one be interested in computing the probability of detection of a UAV flying a specific trajectory, then

the measurement flight should reproduce that trajectory of interest with the best fidelity available.

5.4 Comparison Between Static and Dynamic Results

The differences between the static and dynamic PDF statistics are now investigated. The static measurements used are those taken with a modified Dynamic RCS Measurement System in Section 4.9. The dynamic PDF is Monte-Carlo generated and uses the measurements of Section 5.3.2. All measurements were taken using a VV polarization. Table 5.7 lists the mean in dBsm and the variance in square dBsm of both measurement methods. It shows that the static means and variances are consistently smaller than their dynamic counterparts.

Table 5.7: Comparison of static and dynamic statistics

Freq [GHz]	Static Mean	Dyn Mean	Static Var	Dyn Var
8	−18.52	−16.14	−36.85	−34.79
8.5	−17.92	−15.83	−34.30	−29.16
9	−18.40	−15.55	−35.89	−30.27

Figure 5.25 and 5.26 show the QQ plot of the static versus dynamic quantiles at 8 and 8.5 GHz. Both figures show that the quantiles of the static data sets are consistently smaller than the dynamic quantiles, which implies that both data sets are not drawn from the same random variable.

Figure 5.27 compares the mean of the dynamic PDF within each bin to that of the static RCS at 8.5 GHz. Although the static RCS varies significantly from the mean, it mostly stays within the 5th and 95th percentile of the dynamic PDF of each bin.

The effect of the static measurement methodology is more evident on the probability of detection curves. Figure 5.28 shows the probability of detection based on the PDFs of Table 4.1. The curves show lower probabilities of detection when compared to Figure 5.17. The three static curves are very similar, showing that a frequency change has less impact on the probabilities of detection than in the dynamic case. For example, there is a 1 m difference between the different frequencies for the 90% detection range in the dynamic case, whereas there is only a 0.25 m in the static case.

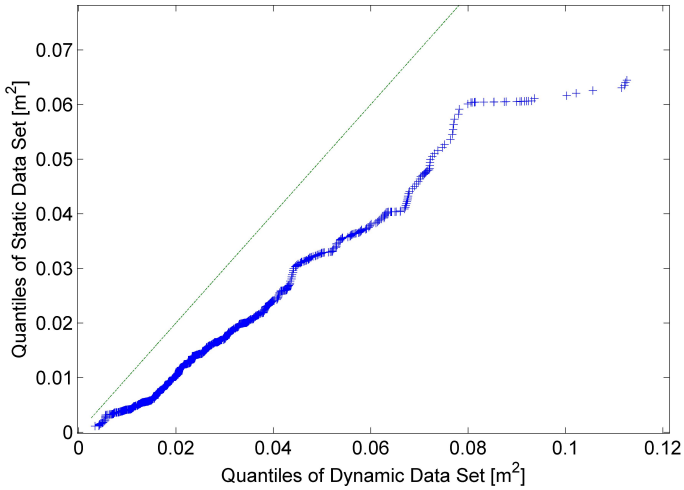

Figure 5.25: QQ plot of static versus dynamic of 8 GHz VV data sets

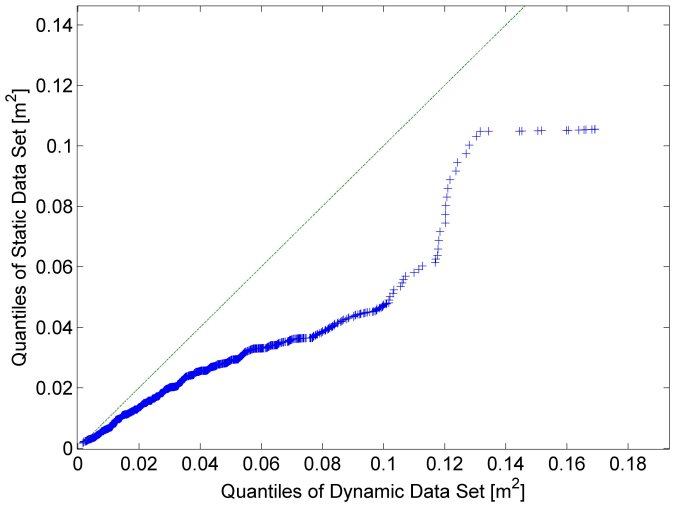

Figure 5.26: QQ plot of static versus dynamic of 8.5 GHz VV data sets

To highlight the differences between static and dynamic results, Figure 5.29 shows the curves for both methods at 8.5 GHz. The probabilities of detection are always higher for dynamic measurements for the investigated ranges.

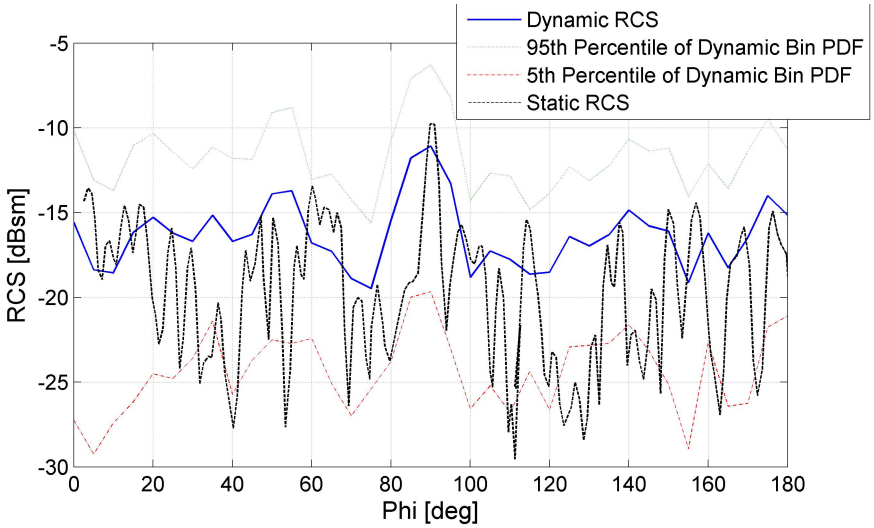

Figure 5.27: Static and dynamic RCS versus yaw angle at 8.5 GHz VV

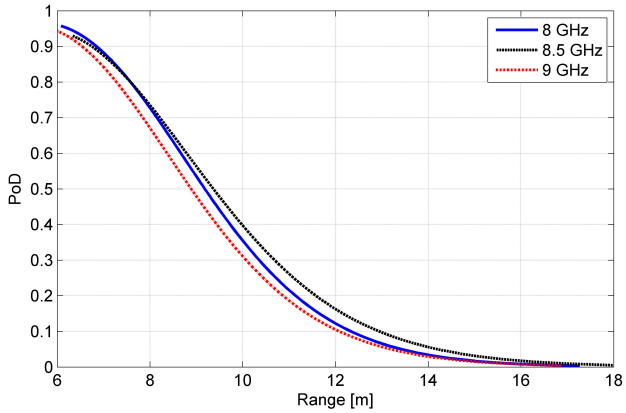

Figure 5.28: Single pulse VV static probability of detection

There are at least two reasons why the quantiles of the static RCS are smaller than their dynamic counterparts. First, the fact that background subtraction could not be used during the dynamic campaign resulted in a higher amount of room clutter. Clutter at the same range as the UAV cannot be removed through time-gating, which reduces the smallest RCS that can be measured.

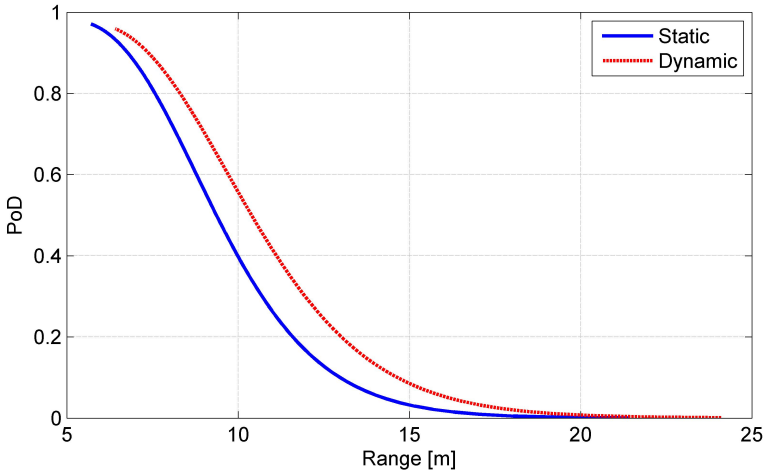

Figure 5.29: 8.5 GHz VV single pulse probability of detection

Second, very small values of RCS occur less frequently in the dynamic case than in the static case due to radar integration. From Figure 3.7, the very low static RCS values occur during sharp nulls of the RCS versus yaw angle curve. However, the Dynamic RCS Measurement System integrates returns during 55.6 ms. Due to vibrations, it is unlikely that the UAV will maintain the exact aspect angle of the nulls for that integration time. Furthermore, the AR.Drone propellers perform a full rotation every 2.1 ms. Even considering the propellers small RCS, the variation of the phase of their contribution should increase the RCS during the integration time. Considering that sharp and deep nulls are not observed dynamically, the reduced dynamic range of the LVRTS when compared to the anechoic chamber (see Figure 4.18) is not a cause for concern, and may even be beneficial.

5.4.1 Notes on The Preferred Measurement Method

Both static and dynamic RCS measurement methods have disadvantages. In the case of static measurements, moving parts and deformations are not accounted for. Therefore, the result is precise, with no guarantee of accuracy. In the case of dynamic measurements, the tracking of the target and clutter increase the number of error sources that corrupt the measurements. Despite attempts to make the result less-dependent upon the flown trajectory with the computation of a full-UAV PDF, vibrations and deformations depend on the

trajectory. Therefore, the dynamically measured RCS may differ on a daily basis. Nevertheless, much faith is placed on dynamic measurements because they represent the *real thing* [6]. Despite their lack of precision, they are very accurate for the exact same conditions as the measurement campaign.

To summarize, static measurements are very precise and error-free, however there are no guarantees that they ever represent the RCS of the target in an operational environment. Dynamic measurements are imprecise and prone to errors, but they are very accurate representation of the RCS during the measurement flight.

The conversion of static to dynamic measurements has been the subject of much studies [9], but no breakthrough could be found within the open academic literature.

5.5 Summary

The Dynamic RCS Measurement System requires careful configuration and calibration, as described in Sections 5.1 and 5.2. The configuration usually represents a trade-off between system efficiency, accuracy and precision. For example, far-field requirements were relaxed based on static ISAR imagery to speed-up measurement and reduce the impact of clutter at higher ranges.

The measurement campaign allowed to compute the RCS PDF using various methods and at different frequencies and polarization. Computing probabilities of detection curves allows an operator to optimize the radar configuration based on the requirements, whether it be highest detection probabilities at short or long ranges.

The repeatability of measurements was investigated by performing two measurement campaigns at 8.5 GHz using a VV polarization. It was shown both campaigns yielded slightly different results. The differences may be explained by the known variations of the dynamic RCS due to changes in trajectories and operating conditions.

Finally, static and dynamic measurements of the AR.Drone yield different full-UAV PDFs. Both the mean and variance of the dynamic PDFs are greater than their static counterparts. This results in an increased probability of detection in the dynamic case, so that the AR.Drone is easier to detect than the static measurements infer.

6 Conclusion

6.1 Summary

As discussed in Chapter 2, measuring the RCS of a target may be done using a variety of methods. Computer simulations can be used or measurements may be taken within an anechoic chamber. The result of both methods is the RCS of the target while it is *at rest* (static). To obtain more operationally relevant data, the RCS of the target may be measured in a dynamic RCS range as the target is flying. This has the advantage of accounting for vibration, deformation and moving parts of the target. However, measurement campaigns become more complex because of the need to track the target in-flight and because the RCS is no longer deterministic.

Conventional methods were used in Chapter 3 to determine the static RCS of the AR.Drone. The results from anechoic chamber measurements and computer simulation show that the RCS varies significantly with aspect angle.

Chapter 4 described the new Dynamic RCS Measurement System and its components. The system uses Optitrack^{TM} infrared positioning data to track the UAV in-flight and to determine its orientation. The LabVolt^{TM} Radar Training System is used to illuminate the UAV and measure its RCS. Post-flight statistical analysis permits the compute of the full-UAV PDF of the RCS and the probabilities of detecting the UAV at certain ranges. The measurement system is validated by comparing static measurements of the UAV taken with the new system to the results of conventional methods of Chapter 3.

The results of a dynamic RCS measurement campaign were presented in Chapter 5. Various statistical ways of computing a representative RCS PDF of the full UAV were shown. The effects of frequency and polarization were investigated, and conclusions were drawn as to the repeatability of measurements. Finally, the static and dynamic RCS measured using the Dynamic RCS Measurement System were compared.

6.2 Conclusions

A new indoor Dynamic RCS Measurement System was successfully designed and implemented at RMCC. Based on a comparison of static measurements taken within an anechoic chamber, it was proven that the new dynamic system is capable of accurately measuring the RCS.

For the first time, the RCS of a drone was measured dynamically at RMCC, resulting in probability of detection curves for various frequencies and polarizations. The results show that there is a difference between the drone static and dynamic RCS, resulting in different probabilities of detection.

The aim of RCS measurement is typically to infer what the RCS of the UAV will be in an operational environment. As such, dynamic measurements are superior as they show a greater resemblance to an operational environment. Nevertheless, the dynamic measurement process has more sources of errors due to the requirement to track the target in-flight and the increased clutter in the uncontrolled environment.

6.3 Contributions

The most important contributions of this work are:

- The design and implementation of a new Dynamic RCS Measurement System;
- The simulation and measurement of the static RCS of the AR.Drone.
- The measurement of the dynamic RCS of the AR.Drone at various frequencies and polarizations.
- The investigation of four techniques to compute a full-UAV PDF of the RCS from dynamic measurements.
- The comparison of the static and dynamic RCS of the AR.Drone.

As a result of this work, RMCC now has the ability to dynamically measure the RCS of mini-drones in an uncontrolled environment. The result of measurement campaigns may be used to infer the probabilities of detection of the UAV by radars operating at the same frequency and polarization.

6.4 Future Work

Areas of this thesis warrant further work and research. A modification to the Dynamic RCS Measurement System should be implemented to speed-up the measurement so that more samples may be acquired. This would increase

the confidence in the fitted PDFs parameters. Similarly, the computation of confidence intervals for the probabilities of detection should be investigated.

The custom antenna turret motion testbed should be replaced with *radar-grade* parts. This would allow the use of background subtraction techniques, making for more precise and accurate dynamic measurements. If the replacement of the motion testbed is not practical, measurements should be re-taken by placing additional microwave absorber on the floor, ceiling and wall.

Finally, a closed-loop controller for the *Turret Controller* should be developed and its effect on the tracking error should be investigated.

Bibliography

[1] C. Uluisik, G. Cakir, M. Cakir, and L. Sevgi, "Radar cross section (RCS) modeling and simulation, part 1: a tutorial review of definitions, strategies, and canonical examples," *Antennas and Propagation Magazine, IEEE*, vol. 50, no. 1, pp. 115–126, Feb 2008.

[2] P. M. Miller, "Mini, micro, and swarming unmanned aerial vehicles: A baseline study." Library of Congress Washington DC Federal Research Division, 2006. [Online]. Available: www.dtic.mil/cgi-bin/GetTRDoc?AD=ADA521374

[3] J. Knowles, "Going small: Jamming the mini-drones," *The Journal of Electronic Defense*, vol. 38, no. 10, pp. 26–30, 2015.

[4] E. Miasnikov, "Threat of terrorism using unmanned aerial vehicles: technical aspects," *Moscow, Russia: Center for Arms Control, Energy, and Environmental Studies, Moscow Institute of Physics and Technology*, 2005. [Online]. Available: http://www.armscontrol.ru/UAV/UAV-report.pdf

[5] N. Mohajerin, J. Histon, R. Dizaji, and S. Waslander, "Feature extraction and radar track classification for detecting UAVs in civillian airspace," in *Radar Conference, 2014 IEEE*, May 2014, pp. 674–0679.

[6] F. T. Cunningham, "The implementation of a dynamic radar cross section measuring technique," Master's thesis dissertation, Naval Postgraduate School, 1971.

[7] J. Silvestro, *Hybrid Finite Element Boundary Integral Method*, ANSYS Inc., (no date cited).

[8] W. du Preez and J. van Schalkwyk, "Processing of dynamic radar cross section measurements," in *Communications and Signal Processing, 1992. COMSIG '92., Proceedings of the 1992 South African Symposium on*, Sep 1992, pp. 29–32.

[9] L. R. Bishop, "The use and misuse of aircraft and missile RCS statistics," DTIC Document, Tech. Rep., 1991. [Online]. Available: http://www.dtic.mil/dtic/tr/fulltext/u2/a239892.pdf

[10] R. M. O'Donnell, *Radar Systems Engineering Lecture 7–Part 1 Radar Cross Section*. MIT Lincoln Laboratory, 2009. [Online]. Available: http://ece.wpi.edu/radarcourse/

[11] M. Lanouette, "Radar cross section of electrically large complex segmented shapes," Master's thesis dissertation, Royal Military College of Canada, 2013.

[12] G. Stimson, *Introduction to Airborne Radar*. Hughes Aircraft Company, 1998.

[13] Richards, M.A., and Scheer, J.A., and Holm, W.A., *Principles of Modern Radar*. SciTech Publishing, Incorporated, 2010. [Online]. Available: https://books.google.ca/books?id=nD7tGAAACAAJ

[14] RCS Calculations Using The Physical Optics Codes. [Online]. Available: http://mail.blockyourid.com/~gbpprorg/mil/radar/pocodes.pdf

[15] L. To, A. Bati, and D. Hilliard, "Radar cross section measurements of small unmanned air vehicle systems in non-cooperative field environments," in *Antennas and Propagation, 2009. EuCAP 2009. 3rd European Conference on*, March 2009, pp. 3637–3641.

[16] *Using the HP8510 network analyzer to make radar cross-section measurements*, HP, 1985, Product Note 8510-2.

[17] E. Knott, J. Shaeffer, and M. Tuley, *Radar Cross Section: Its Prediction, Measurement, and Reduction*, ser. Artech House radar library. Artech House, 1985. [Online]. Available: https://books.google.ca/books?id=SAtTAAAAMAAJ

[18] PNA Series Network Analyzers Help. [Online]. Available: http://na.support.keysight.com/pna/help/latest/help.htm/

[19] C. Ozdemir, *Inverse Synthetic Aperture Radar Imaging With MATLAB Algorithms*, ser. Wiley Series in Microwave and Optical Engineering. Wiley, 2012. [Online]. Available: https://books.google.ca/books?id=615p9BKjeW0C

[20] W. Shi, X.-W. Shi, and L. Xu, "RCS characterization of stealth target using chi-square distribution and lognormal distribution," *Progress In Electromagnetics Research M*, vol. 27, pp. 1–10, 2012.

[21] H. Akaike, "A new look at the statistical model identification," *Automatic Control, IEEE Transactions on*, vol. 19, no. 6, pp. 716–723, Dec 1974.

[22] W. M. Duckworth and W. R. Stephenson, "Beyond traditional statistical methods," *The American Statistician*, 2012.

[23] N. Currie, *Radar Reflectivity Measurement: Techniques & Applications*, ser. Artech House radar library. Artech House, 1989. [Online]. Available: https://books.google.ca/books?id=_AJTAAAAMAAJ

[24] A. El-Shaarawi and A. Naderi, "Statistical inference from multiply censored environmental data," *Environmental Monitoring and Assessment*, vol. 17, no. 2, pp. 339–347, 1991.

[25] D. Shnidman, "Calculation of probability of detection for log-normal target fluctuations," *Aerospace and Electronic Systems, IEEE Transactions on*, vol. 27, no. 1, pp. 172–174, Jan 1991.

[26] Parrot AR.Drone User Manual. [Online]. Available: http://ardrone2.parrot.com/support/

[27] O. Osorio. (24 Feb 2016) Ar Drone 2.0 with Indoor Hull. [Online]. Available: https://grabcad.com/library/drone-2-0

[28] HiQ Motion Tested Specification Sheet. [Online]. Available: www.quanser.com/products/docs/1832/hiq

[29] (2016) ANSYS HFSS Brochure. [Online]. Available: http://resource.ansys.com/staticassets/ANSYS/staticassets/resourcelibrary/brochure/ansys-hfss-brochure-16.0.pdf

[30] 8096 Radar Training System. [Online]. Available: https://www.labvolt.com/search/?q=datasheet_98%208096%200_en_120V_60Hz%20pdf

[31] Tracking Tools 2.4.0 User Guide. [Online]. Available: http://www.optitrack.com/downloads/tracking-tools.html

[32] Digital Phosphor Oscilloscopes User Manual. [Online]. Available: http://www.tek.com/oscilloscope/mso4000-dpo4000-manual/mso4000b-and-dpo4000b-series-0

[33] High Power Amplifier - ZVE-3W-183+. [Online]. Available: http://www.minicircuits.com/pdfs/ZVE-3W-183+.pdf

[34] (2015) Limits of human exposure to radiofrequency electromagnetic enegy in the frequency range from 3 khz to 300 ghz. Health Canada. [Online]. Available: http://www.hc-sc.gc.ca/ewh-semt/pubs/radiation/radio_guide-lignes_direct/index-eng.php

[35] Agilent 33210A 10 MHz Function Arbitrary Waveform Generator. [Online]. Available: http://sdphca.ucsd.edu/Lab_Equip_Manuals/hp_33210a_User_guide.pdf

[36] Model 3160 Series Pyramidal Horn Antenna User Manual . [Online]. Available: www.ets-lindgren.com/manuals/3160.pdf

[37] MPS-3005L-3 Specifications. [Online]. Available: http://www.tme.eu/en/details/mps-3005l-3/multichannel-power-supplies/matrix/

[38] E. Knott, J. Shaeffer, and M. Tuley, *Radar Cross Section, Second Edition*, ser. Electromagnetics and Radar Series. Institution of Engineering and Technology, 2004. [Online]. Available: https://books.google.ca/books?id=j7hdXhgwws4C

[39] S. Aich, C. Ahuja, T. Gupta, and P. Arulmozhivarman, "Analysis of ground effect on multi-rotors," in *Electronics,Communication and Computational Engineering (ICECCE), 2014 International Conference on*, Nov 2014, pp. 236–241.

[40] ECCCOSORB AN Polarizations. [Online]. Available: http://www.eccosorb.com/Collateral/Documents/English-US/Electrical%20Parameters/an-anw%20polarizations.pdf

[41] HS-5245MG Digital Mini. [Online]. Available: https://www.servocity.com/html/hs-5245mg_digital_mini.html#.VqePwquKBaR

[42] Instrument Control Toolbox Documentation. [Online]. Available: http://www.mathworks.com/help/instrument/index.html

[43] Canadian Forces School of Aerospace Warfare, "Advanced operational electronic warfare book 2," Version 1302.

[44] D. Hess, "Introduction to rcs measurements," in *Antennas and Propagation Conference, 2008. LAPC 2008. Loughborough*, March 2008, pp. 37–44.

[45] R. D'Agostino, *Goodness-of-Fit-Techniques*, ser. Statistics: A Series of Textbooks and Monographs. Taylor & Francis, 1986.

[46] L. Bantis. (18 Sep 2012) Fit distributions to censored data. [Online]. Available: http://www.mathworks.com/matlabcentral/fileexchange/38226-fit-distributions-to-censored-data

[47] N. Mehta, J. Wu, A. Molisch, and J. Zhang, "Approximating a sum of random variables with a lognormal," *Wireless Communications, IEEE Transactions on*, vol. 6, no. 7, pp. 2690–2699, July 2007.

[48] CPDL-100A Programmable Delay Line Operating and Programming Manual. [Online]. Available: http://www.colbyinstruments.com/cpdl-100a/